“BABEŞ-BOLYAI” University

Faculty of Physics

Physical Doctoral School

Preclinical studies of magnetic resonance imaging at 7 T and on some rare earth contrast agents

-PhD Thesis Summary-

Scientific advisor:

Prof. Dr. Simion SIMON

PhD Student:

Farcașanu Alexandru Ștefan

Cluj-Napoca

2022

Content

Introduction

Preclinical MRI imaging investigations, both in vivo and in vitro, have proven to be extremely important, being in many cases a precondition for the transition to clinical research. In preclinical research using ultra high magnetic fields, it is not necessary to use contrast agents, a necessity that is required in clinical imaging studies at lower magnetic fields.

The versatility of using the RM imaging technique in preclinical studies has been demonstrated in both ex vivo and in vivo research studies. The information obtained through the use of this technique allowed for highlighting the different stages of development of the human nervous, system, but also its use for the post-mortem diagnosis of embryonic congenital malformations being an alternative to classical autopsy. Preclinical in vivo research has also shown that the use of the MRI technique is necessary regardless of whether the pathologies or pharmacokinetics of some drugs are studied on the animal model.

Silica particles doped with paramagnetic Dy and Gd ions have been successfully synthesized using chemical synthesis based on the modified Stöber method, with potential applications as contrast agents for magnetic resonance imaging (MRI).

Structural characterization analyses show an amorphous particle structure character (XRD), good thermal stability (DTA/TGA) and a spheroid shape (SEM), (TEM). Hydrodynamic stability has been demonstrated by potential Zeta analysis and DSL. The integration of Dy and Gd ions into the silica network has been demonstrated by MAS-NMR, EPR and FTIR spectroscopies.

Magnetic resonance relaxation (R-MR) examinations of the samples indicate a high rate of relaxivity for Dy-doped particles, making them suitable as a contrast agent for T2 magnetic resonance imaging. This is in contrast to the results obtained on Gd-doped particles that are an effective contrast agent for MRI T1. In particular, if the silica structure incorporates both Gd and Dy, the particles obtained are suitable for improving contrast in T1 and T2 weighted images. These characteristics of the samples are also supported by the value of the relaxivity ratio (r2/r1) for the three samples doped with paramagnetic ions. The results confirm the sustainability of MRI contrast agent applications in both T1-weighted and T2-weighted imaging for all three synthesized samples.

Chapter 1

Magnetic resonance imaging (MRI) is the non-invasive diagnostic method, without using ionizing radiation, for clinical trials and preclinical research. MRI is an imaging technique that allows obtaining images with high contrast and spatial resolution, especially of soft tissues [1].

The quality of the information obtained in the investigation of soft tissues, using MR imaging, made this technique to be successfully used for the investigation of the central nervous tissue at different stages of embryo development [2], [3], [4] but also in the case of embryonic pathology studies [5] .

In the case of preclinical animal studies, the MRI imaging technique has a great advantage both from an ethical point of view, since animals are not slaughtered in the study, and from the point of view of the quality of the information obtained in the experiment. The relevance of MR imaging in preclinical studies has been demonstrated in various interdisciplinary experiments conducted with the preclinical MR scanner of 7T [6], [7], [8], [9].

The signal-to-noise ratio and therefore the spatial/temporal resolution natively increases with the magnetic field strength (>3 T), these field intensities being used especially in preclinical applications. In clinical diagnosis, the moderate intensity of the magnetic field (0.5–3 T) predominates, which leads to the need to use contrast agents that play an increasingly important role to increase image sensitivity by improving contrast in regions of interest (ROI) [10].

In MRI, the relaxation time is measured (T1 - longitudinal relaxation time, T2 - transverse relaxation time) [11]. The MRI signal tends to increase with the shortening of T1 and decreases with the shortening of T2 [12].

Contrast agents are used to alter proton relaxation rates and improve the visualization of differences between normal and diseased tissues [13] [14]. Depending on how the contrast changes are changed, contrast agents are divided into positive contrast agents (T1) they produce an increase in signal intensity in the region of interest (ROI) (areas with hyper-signal -brighter images) in T1-weighted images.

A second category of contrast agents are negative ones, their presence produces a decrease in signal intensity in ROI (areas with hypo signal-image darker) in T2-weighted images [15]. And

the third category of contrast agents are the dual ones where two different simultaneously weighted imaging modes T1 and T2 [16] are used.

The most used contrast agents in the clinical diagnosis are composed of Gd ions, it has a positive effect in the rm images being T1-weighted; an effect that is due to the 7 unpaired electrons (the effective magnetic moment is 7.29 μB) that disrupts the relaxation of protons in neighboring tissue resulting in an efficient shortening of the longitudinal relaxation time and an increase in the intensity of the magnetic resonance signal [17] [18].

Dy3+ based compounds that have an effective high magnetic moment (10.6 μB) and present a short electronic relaxation time (approximately 10-13sec) allow protons to be relaxed in ultra-high magnetic fields and are thus a negative contrast agent (T2) [18]. It induces the relaxation of T1 to a negligible extent, since the orbital movement with 4f electrons is much faster than the slow movement of the proton spin. While the spin motion of the electron 4f in Gd3+ fits closely with the slow relaxation of the proton spin. Therefore, Dy3+ is not suitable for T1 MRI contrast agents, but is suitable for T2 MRI contrast agents in different nanoparticle forms because of the magnetic moment value of particles containing Dy3+ at room temperature. Relaxation of T2 is only related to the total magnetic moment of a contrast agent, since it is mainly induced by the fluctuation of a local magnetic field generated by the contrast agent [19] .

More recently, the growing demand for contrast agents has prompted attempts to combine T1 and T2 imaging in a synergistic manner to avoid possible RM [20] artifacts and improve sensitivity because T1–T2 combined imaging modes can allow cross-validation of the data obtained, producing complementary and self-confirmed information for high accuracy and sensitivity [21].

Mesoporous silica spheroid particles offer a multitude of advantages such as increased porosity, easy surface functionalization, biocompatibility, low toxicity, being easy to manufacture with relatively low-cost procedures and are ideal for hosting molecules in a wide range of sizes, shapes, and functionalities [22][23]. The Stober method [25] is a classic approach to the synthesis of spherical silica particles and has been used to synthesize these spheroid particles with the addition of Gd3+ and Dy3+ ions.

The goal of these parts of the study was the synthesis of microspheres of SiO2 doped with Gd3+ and Dy3+ ions in order to be used as contrast agents in magnetic resonance imaging.

After the Introduction, Chapter I presents the fundamental principles of what implies nuclear magnetic resonance, being presented the physical phenomena such as nuclear spin, the Zeeman effect but also the two most important parameters that characterize the energy absorption of nuclear thorns, namely the spin-network relaxation time and the spin-spin relaxation time, the latter being the parameters that characterize the spin systems. It also presents the mathematical transformation of signals and their spatial distribution into a virtual mathematical space.

Chapter III presents how the transition is made from information in the form of spectra to information in the form of images; both the components that are necessary for this transformation and the physical principle that involves the spatial encoding of information are presented. Within this chapter are exposed to the necessary properties that a biomaterial must fulfill in order to qualify for contrast agent in MRI imaging.

In the chapter, IV is presented the interdisciplinary preclinical investigations carried out with the MRI 7T scanner and the results obtained by using these techniques in the study of the human nervous system - ex vivo human embryo research; investigated by post-mortem MRI for congenital malformations; demonstrates that MRI is a useful tool for imaging anatomical conditions of the morphology of the external and internal root canal for endodontic purposes. In the second half of this chapter are exposed to the results of MRI techniques uses in in vivo studies: integration of the biomaterial into the tissue after implantation and periodic follow-up of this process; morphological investigation of venomous glands in the case of Ameiurus nebulosus species; follow-up of inflammatory processes in case of induction of periapical dental lesions and study of pharmacokinetics with lutein in the case of experiment on an animal model.

Chapter V presents, in the first part, in detail, the method of synthesis of silica spheroids doped with paramagnetic ions, this being the classical Stober method modified so as to obtain these materials with the physical properties necessary to be contrast agents in RM imaging.

In the second part of Chapter V are presented the experimental results obtained by using the experimental techniques presented in the previous chapter, which were necessary for the determination of the physical properties of the new synthesized materials.

Chapter VI are presented the conclusions of the research that incorporate the results obtained using MRI imaging. In vivo and ex vivo experiments, the versatility of the use of this technique in

preclinical research and its importance in these studies has been demonstrated. And in the case of the study of rare earth contrast agents, the initial hypothesis of the research was confirmed by the results obtained. In this chapter, there are also the perspectives of continuing this research that can ultimately lead to obtaining a biomaterial that can be used in MRI imaging as a dual contrast agent.

This paper ends with the presentation of the scientific results held during these years of research and not least with thanks to the people who supported me in carrying out this research.

Chapter 4. Preclinical studies of magnetic resonance imaging at 7 T

In the research, using the RM technique, the multidisciplinary approach was a necessary and facile one, which at the same time supports the development of new directions of application of this technology that led to obtaining outstanding results in embryonic research. One such interdisciplinary research approach is the ex-vivo studies of diagnosis and follow-up of the development of the nervous system at different stages of embryonic development without altering the samples.

In vivo research conducted on animals without affecting their integrity, is an important asset of the RM imaging technique, and this type of research is carried out within multidisciplinary collaborations, involving collectives in the field of human and veterinary medicine.

Bruker Biospec 7.0 Tesla Scanner

The Biospec scanner has the ability to provide, non-invasively, a wealth of functional and anatomical information in vivo. State-of-the-art MRI cryoprobe technology combined with USR magnets provides high spatial resolution, allows imaging and spectroscopy on 1H and a number of other MR-active nuclei such as 31P, 23Na, 19F and 13C. Examples of studies that can be conducted with the BioSpect 70/20 USR system include:

- ✓ "Classical" images based on T1, T2 or proton density are usually used to show anatomical details.
- ✓ Blood flow in the arteries or veins (magnetic resonance angiography or MRA);

- ✓ Vascularization of blood through the tissues, giving the map of cerebral blood flow (CBF) and cerebral blood volume (CVD).
- ✓ Molecular diffusion of water through tissues, (tractography and dissemination of tensor images (DTI)),
- ✓ The relative degree of water bound and not connected by contrast transfer of magnetization (MTC).
- ✓ Movement of tissues, such as the activity of the heart that results in the measurement of the ejection frequency and the movement of the myocardium.
- ✓ Temperature in tissues and intracellular pH measurements.
- ✓ Oxygenation of the blood to show the areas of the brain activated by stimuli - functional MRI (fMRI);
- ✓ Changes in blood vascularization through tissues in response to pharmacological treatment (phMRI);

Ex-vivo studies

Understanding the morphogenesis of organs at various stages of development provides an insight into the mechanisms of development of congenital anomalies. Magnetic resonance techniques are effective methods for obtaining detailed morphological data of embryos.

Micro-MRI of human embryos is a relatively new method of morphological research in the field of modern embryology. It provides precise details of the developing embryo thanks to a spatial resolution of up to 20 μm/pixel [2].

The MRI imaging research on embryos was carried out through collaboration with the embryology department of the "Iuliu Haţieganu" University of Medicine and Pharmacy in Cluj-Napoca.

The first study of this embryonic research approach was aimed at the morphological characterization of the developing brain of aborted, two-stage Carnegie embryos with the help of anatomical examination, along with magnetic micro-resonance imaging.

The two embryos were examined and photographed by transilumination. Magnetic resonance analysis was performed using a Bruker Biospec 7.04 Tesla scanner (Ettlingen, Germany). Protocols based on a 2D T2-weighted sequence were used to morphologically analyze embryos in the three anatomical planes.

2D axial scanning was performed with a slice thickness of 300 microns and different distances between the slices. By reducing the field of view to a value of just 20% above the largest 2D axial fingerprint and increasing the number of averages to 32, an excellent resolution of 20μm/voxel was achieved.

In our study [2], remarkable spatial resolutions of 20μm/voxel were obtained, which provide highly accurate images (Figure 4.1). The surprising details of developing brain morphology can be seen on RM slices, making this imaging technique a new standard method in morphological studies. In addition, RM is reproducible and does not destroy anatomical specimens as histological methods do.

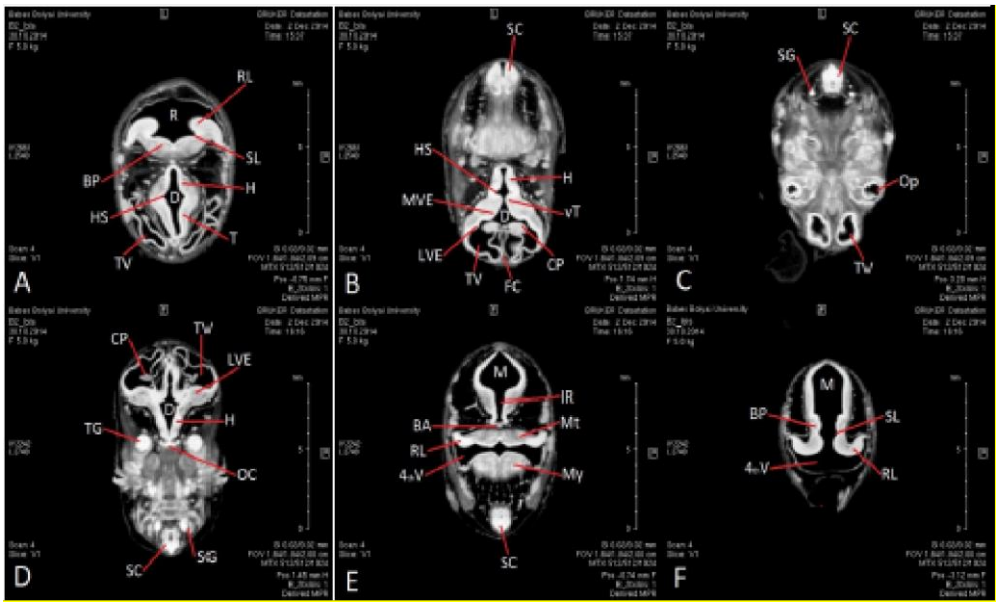

Figure 4.1. Human embryo 22 mm CRL, CS 21 illustrated by micro-MR. Axial (A-C) and coronal (D-E) sections are presented. TV: telencephalic vesicles, FC: falx cerebri, D: diencephalon, M: midbrain, R: fourth ventricle, CP: choroidal plexuses, H: hypothalamus, T: thalamus, HS: hypothalamic sulcus, LVE: lateral ventricular eminence, MVE: medial ventricular eminence, Mt: methencephalon, RL: rhombic lips, SL: sulcus limitans, BP: basal plate, BA: basilar artery, SC: spinal cord, SG: spinal ganglion , vT: ventral thallus, Op: optical cup, TG: trigeminal ganglion, OC: optic chiasma, IR: rhombencephal isthmus, Myelencephal.

A second ex vivo study [5] conducted involved the use of post-mortem MRI imaging (PM-MRI) as a promising alternative to the conventional autopsy, one of the advantages of this method being the possibility of improved fetal morphological evaluation without altering the integrity of the embryo.

The current study presents the case of a fetus diagnosed with Down syndrome at 13 weeks of gestation (Figure 4.3). Fetal abnormalities were analyzed by prenatal ultrasound, PM-MRI and conventional autopsy.

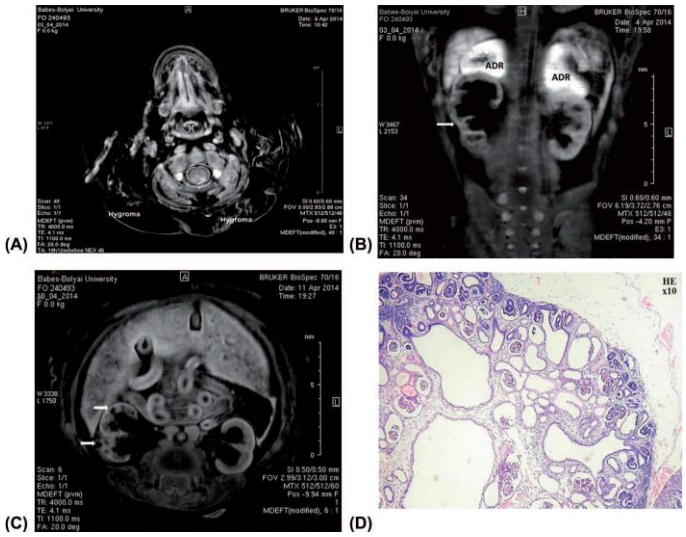

Figure 4.3. (A) Axial MRI-T1 IR WI head of a 13-week-old male fetus, representing a cervico-dorsal hygrom. (B) Coronal T1 IR WI of a male fetus of 13 weeks, centered on the abdomen: arrow indicating a kidney as abnormal: sinus relaxed, cortical thicknesses diminished, (ADR adrenal glands). Note the left kidney: smaller and located at the same level as the right one. (c) Axial T1 IR WI centered on the kidneys. Arrows on the right kidney indicate small cystic structures in the renal cortical. (D) Section through the right kidney. Multiple cystic dilations of nephron components (HE 10X).

Using high-performance PM-MRI as an alternative, or in addition to conventional autopsy in fetuses of early gestational age, it becomes possible to identify subtle, otherwise overlooked malformations. Advanced imaging studies can help improve pathological analysis and prenatal diagnosis, facilitating additional patient counseling and fetal care. The third ex vivo research [4] on embryos aimed to evaluate the growth and development of the cerebellum using 2 different measurement techniques: MR imaging and ultrasound technique. The measurements of the cerebellum were a function of the gestational age. 14 corresponding aborted human fetuses were studied at 15-28 weeks of gestation, preserved in a 9% formol solution. Adjustments to anatomical references were obtained through T2 (T2-wi) weighted images in the three orthogonal planes: axial, coronal, and sagittal planes. For the acquisition of 3D images of the nervous system, the Fast Imaging with Steady-state Precession (FISP) pulse sequence (Figure 4.2) was used.

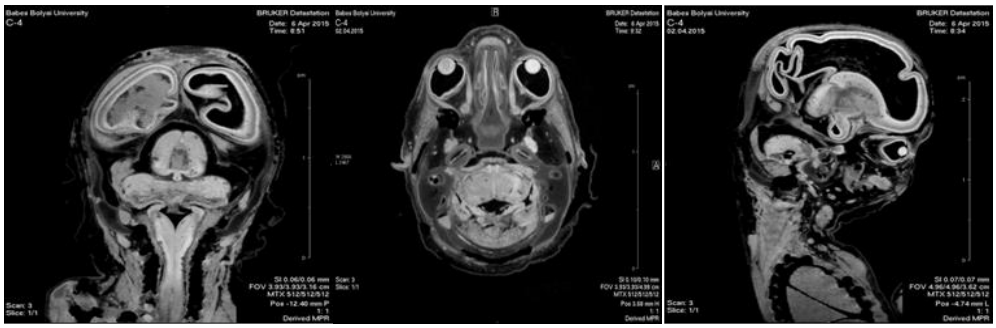

Figure 4.2. Fetus 15 GW - RM images of the axial, coronal and sagittal planes.

The results showed that there is a linear correlation between RM measurements and ultrasonic determinations. Based on all the data collected we could apply the formula of the transverse ellipsoid for calculating the cerebellar volume, a useful criterion in evaluating the development of the cerebellum and the gestational age. Embryology studies are still needed for a full evaluation of developing organs. They can provide a better understanding of normal and pathological morphogenesis.

The fourth research [3] of imaging MR on embryos aimed at the morphological description of ganglion eminences within the embryonic and early fetal brains, by using MR imaging (Figure 4.3).

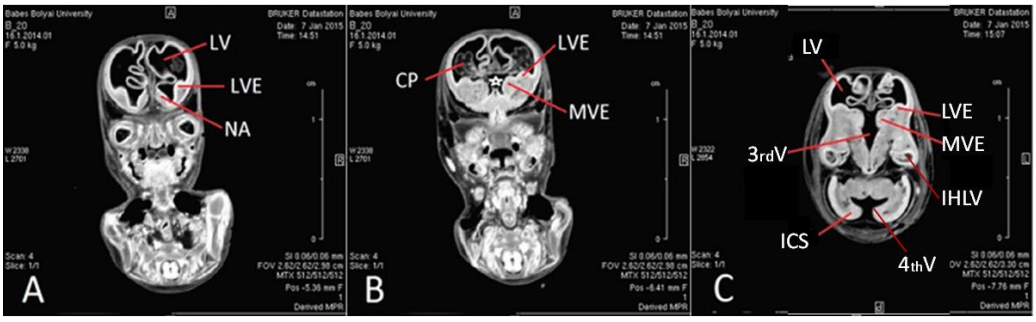

Figure 4.3. Human embryo 32 mm CRL, 10 GW, CS 23. Coronal (A, B) and axial (C) slices are shown. VS: lateral ventricle, LVE: lateral ventricular eminence, NA: nucleus accumbens, CP: choroid plexus, 3rdV and star in (B): third ventricle, ICS: internal cerebellum swelling, IHLV: inferior horn of the lateral ventricle, 4thV: fourth ventricle.

This technique provides clear images of small nervous structures, such as ganglion eminences. We can hope that improving the spatial resolutions of MRI machines by using more intense magnetic fields will provide "histological" images of tissues, either in 2D slices or in 3D reconstructions. All these studies have demonstrated the ability of MR imaging with a magnetic field of 7T to provide important information in the study of embryonic development. Another type of ex vivo study [26] conducted using the MR imaging technique aimed to demonstrate that magnetic resonance imaging is a useful tool for imaging the anatomical conditions of the morphology of the external and internal root canal for endodontic purposes. The current ex-vivo experiment shows the precise reconstruction of the 3D volume (Figure 4.4) of the internal and external morphology of a human tooth extracted and treated endodontically using a set of image data obtained by magnetic resonance imaging.

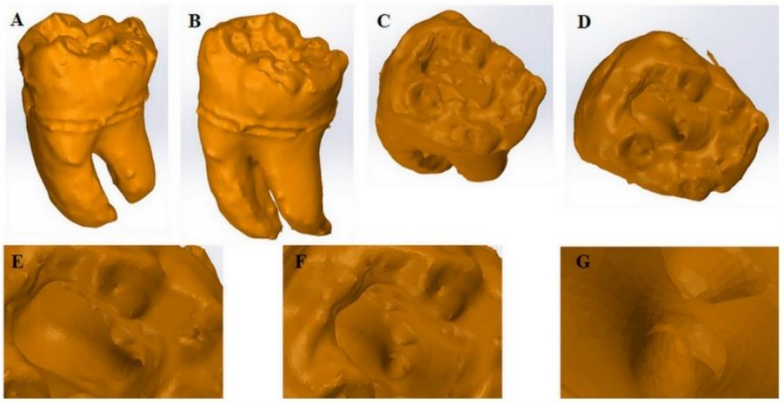

Figure 4.4 Reconstitution of the surface filled in 3D volume. A. External lingual vision; B. External vestibular vision; C. Occlusal view of the pulp chamber; D. Access cavity; E. View of the opening of the distal canal, on the floor of the pulp chamber; F. Opening of the distal root canal (foreground); G. View inside the coronal third of the root canal.

MR imaging provides datasets of 3D images with more information than conventional radiographic techniques. Due to its imaging capacity of both hard and soft dental tissues, MRI imaging can be successfully used as a 3D diagnostic imaging technique in dentistry. When choosing the imaging method, dentists should weight the benefit-risk ratio, taking into account the costs associated with magnetic resonance imaging and the harmful effects of ionizing radiation when using conical beam computed tomography or conventional radiography.

In vivo studies

In vivo, preclinical studies are the biggest advantage in using this RM imaging technique, as they do not affect the integrity of the animal that is part of the study and do not use ionizing radiation that would lead to other effects on the guinea pig.

One of the studies [6] highlighted the integration and regeneration of bone after implantation of a biomaterial in bone tissue (left and right femur of the guinea pig), but also the follow-up of this periodic process without affecting the integrity of the rat. To follow the evaluation of implanted materials, MRI experiments were conducted. MRI scans were performed at different time intervals: the first MRI investigation was performed after surgical implantation of the composite scaffolding (Figure 4.5) and the initial bone defect can be observed; the second was performed 5 days after implantation (Figure 4.6, 4.7), while the last was performed 28 days after surgery.

The MRI experiment allowed non-invasive and non-destructive observation in vivo of bone development without affecting the final results.

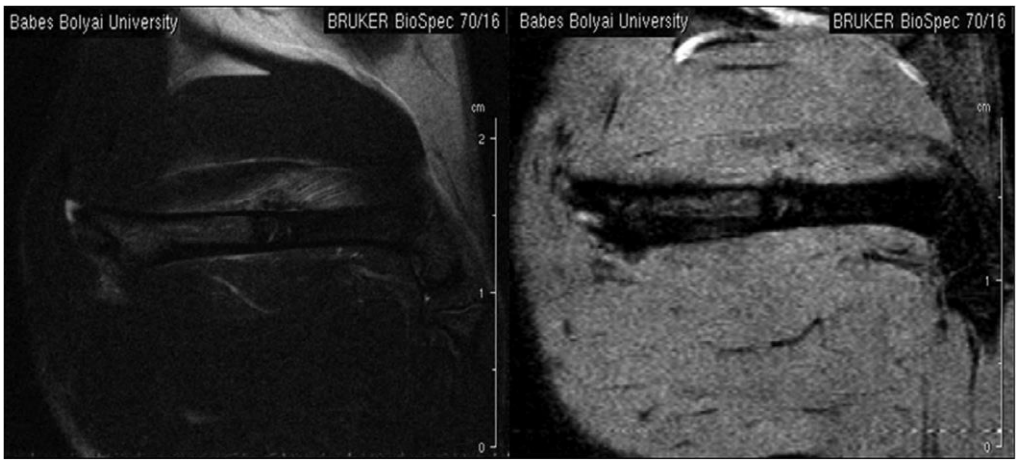

Figure 4.5. MRI images obtained immediately after surgery (a, RARE protocol left; b, right FLASH protocol).

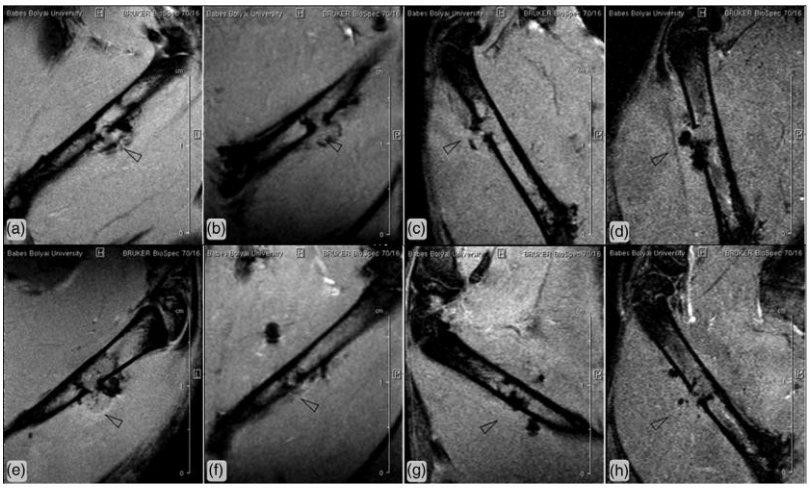

Figure 4.6. MRI images obtained 5 days after the surgery: the first line representing the right leg of each Alg-Pll-0,5CuBG group (a), Alg-Pll-1,5CuBG (b), Alg-Pll-BG (c), Alg-Pll (d) and the second line representing the left leg of each Alg-Pll-βTCP/HA group (e, f, g, h).

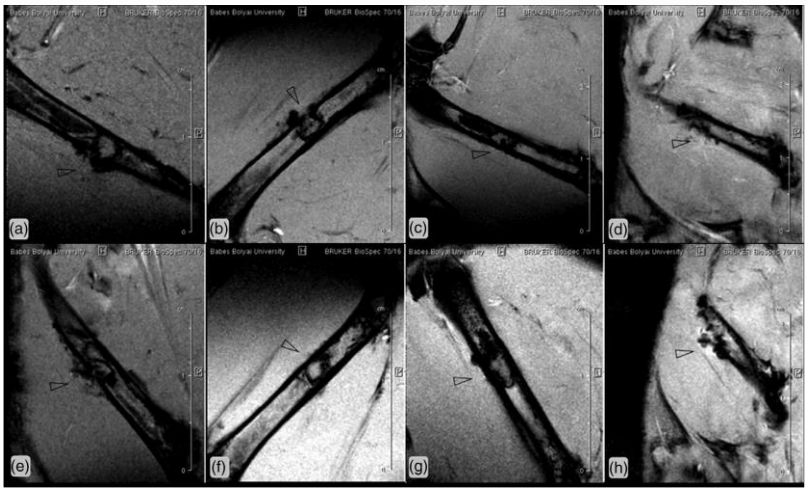

Figure 4.7. MRI images obtained 5 days after the surgery: the first line representing the right leg of each Alg-Pll-0,5CuBG group (a), Alg-Pll-1,5CuBG (b), Alg-Pll-BG (c), Alg-Pll (d) and the second line representing the left leg of each Alg-Pll-βTCP/HA group (e, f, g, h).

Another morphological MRI imaging study was performed on the species Ameiurus Nebulosus [7], where we investigated the form and topography of the venomous glands. The main reason for this investigation was to provide a better understanding of the defense mechanism of this species.

For the anatomical RM imaging investigations, the RARE (Rapid Acquisition with Refocused Echoes) and Turbo RARE High-Resolution protocols were used, based on the echo RF pulse sequence.

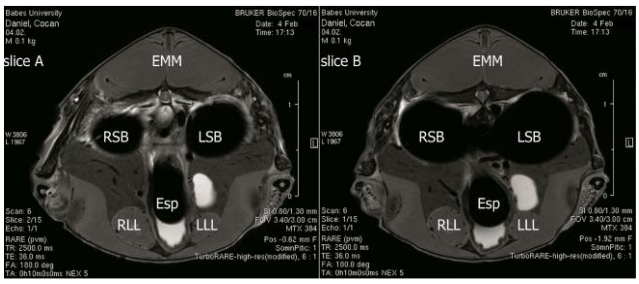

Figure 4.8. Axial section of Ameiurus nebulosus. Cranial section scanned to the first dorsal fin. A, slice 2/15; B, slice 1/15.

The use of MRI techniques for anatomical investigations of venomous glands in Ameiurus Nebulosus has proven to be very accurate, both in identifying the shape and topography of the venomous glands. Also, by using MRI techniques we have highlighted the complex defense mechanism that developed against predators.

The in vivo study aimed to highlight the qualitative changes detected by the imaging of RM 7 T and micro-CT in the animal model to which periapical lesions were experimentally induced. All animals were investigated at 14, 30 and 60 days using MR imaging, and periapical inflammation was revealed, which was visible early in the axial MRI (Figure 4.9.a) and coronal (Figure 4.9.b) sections (Figure 4.9.b).

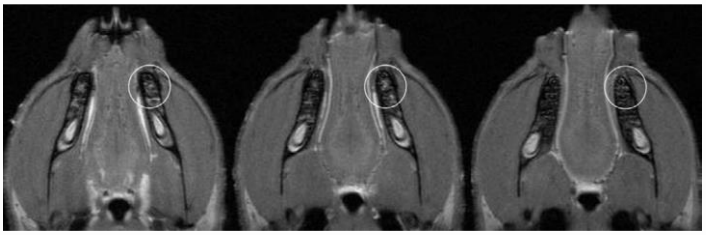

Figure 4.9.a. Sequences successive MRI axial mandibular molars, for 30 days.

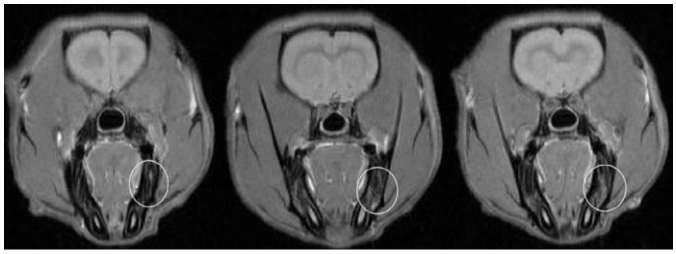

Figure 4.9 Successive MRI sequences of mandibular coronal molars, time 60 days.

The study that analyzes the famacocynetics of some drugs necessary for the treatment of eye problems using MRI Imaging (MRI) [9], this technique has evolved into a multifunctional, non-invasive tool that serves in both the preclinical and clinical environment. It can be used in a safe and non-invasive way for in situ, real-time visualization, high-resolution localization and quantification of ophthalmic drugs when administered, with or without contrast agents. Unlike conventional anatomical imaging by RM, magnetic resonance spectroscopy (MRS) (Figure 4.10) measures information about the chemical change of individual molecules in a living subject, allowing monitoring of various biochemical and metabolic processes in comparison and when administering a bioactive of interest.

The present study, using a 7 T MRI Scanner Bruker Biospec 70/16 USR, investigated the ocular biodistribution in adult rats of lutein administered topically in the hydrogel matrix using the MRS method. Comparative intra- and interindividual studies (treated vs. untreated eyes; hydrogel with and without lutein; healthy vs. sick - diabetic retinopathy; etc.) were conducted to validate the applicability of this MRS technique in demonstrating the capacity of locally administered lutein. in touching the targeted retinal tissue.

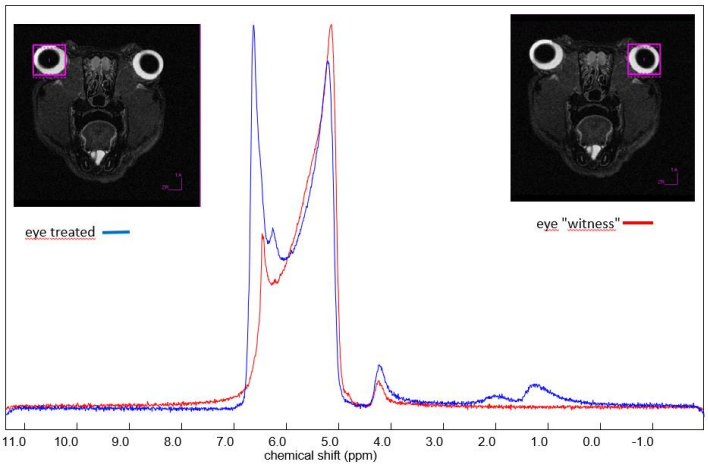

Figure 4.10. MRS spectra on the treated and untreated eye

In imaging experiments MR preclinical the need to use contrast agents is not so high compared to diagnostic and research investments in the field of clinical MR imaging. This is due to the use, in preclinical studies, of much higher magnetic fields compared to the clinical ones. For this reason, arises the need to create a contrast agent for clinical trials, but as is normal in the first stage preclinical research is mandatory for a new contrast agent in MR imaging.

Chapter 5. Study of contrast agents with rare earth

5.1 Synthesis of spheroid particles and structural characterization methods

Synthesis of materials by the Stober method

In the synthesis of systems based on SiO2 with the addition of paramagnetic ions (Gd and Dy) was used for the preparation of the modified Stober method [25] [27], thus four samples were obtained as follows:

- **P0:** 100% SiO_2
- **P1:** 99%$Si0_2$ 1%Dy_20_3
- **P2:** 99%$Si0_2$ 1%Gd_20_3
- **P3:** 99%$Si0_2$ 0.9%Dy_20_3 0.1%Gd_20_3

The SiO2 (P0) system was prepared by mixing a mixed solution of ethanol (160ml) and distilled water (100ml) to which 1g of dodeciamine (DDA) was added, and after homogenization of the solution 10ml TEOS was added. This mixture was made at room temperature. The solution was stirred for 3 hours, then the precipitate obtained was separated from the solvents by centrifugation. The product was washed with distilled water and ethanol twice and then centrifuged. The resulting sample was dried in an incubator at 37 °C for 72 hours and 24 hours at 60 °C to remove water and solvents.

In the case of systems to which paramagnetic ions were added, a third solution consisting of 10 ml H2O and nitrates (0.314 g DyN3O9 · xH2O for sample P1, 0.229 g [Gd(NO3)3]+6H2O for sample P2 and for sample P3 were 0.04 g (Gd(NO3)3)+6H2O was introduced into the preparation protocol, 0.311 g DyN3O9 · xH2O). This was added simultaneously with TEOS in the mixed solution of ethanol distilled water and DDA, after which the process was identical to that of sample synthesis P0. Figure 5.4 exemplified the brewing scheme for the P3 solution.

Finally, the sample was calcined to 600 °C for 1 hour in an electric furnace, in an air atmosphere and cooled to room temperature. The heating rate of the furnace up to 600 °C was 5 °C/min.

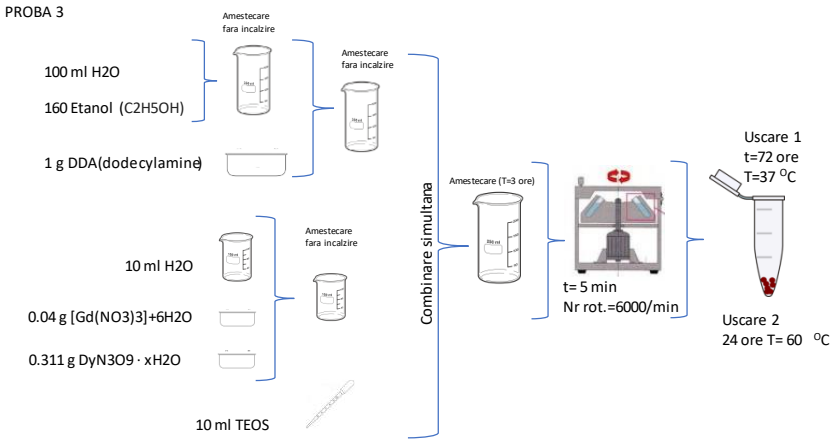

Figure 5.4. P3 sample preparation scheme

Relaxometry by Magnetic Resonance Imaging

For information processing and obtaining relaxation times (T1 and T2) were used ParaVison5.1 (Bruker BioSpin MRI GmbH, Ettlingen, Germany) and Parametric MRI (pMRI) software[31] in which roi were selected and thus obtained their values. The graph in which the measured easing rate is represented (1/Ti, where i=1, 2) in relation to the contrast agent concentration, in order to determine the relaxivity by calculating the linear regression slope was made using originlab software [32].

5.2. Experimental results on rare earth contrast agents

Differential thermal analysis

Based on the DTA/TGA thermograms of samples P0, P1, P2 and P3, the heat treatment temperature was established to achieve structural stabilization of the samples. The thermal behavior of the prepared samples was investigated by measurements with the DTG-60H Shimadzu derivatograph.

The resulting thermograms are shown in Figure 2 and the corresponding event assignments are shown in Table 6.1.

Sample	Temperature range (º C)	Temperature Events (º C)		Weight loss (%)	Total weight loss (%)
		Endo	Exo		
P0	20-165	90	-	-13	-28.85%
	165-295	-	288	-10.5	
	295-500	-	376	-3.5	
	500-700	-	-	-1.85	
	700-1100	-	720	-	
P1	20-165	74	-	-9.8	-21.20%
	165-295	-	-	-6.8	
	295-500	-	-	-2.9	
	500-700	-	-	-1.7	
	700-1100	-	720	-	
P2	20-165	62	-	-18	-32.50%
	165-295	-	293	-10.5	
	295-500	-	-	-2.4	
	500-700	-	-	-1.6	
	700-1100	-	720	-	
P3	20-165	100	-	-8.5	-23.50%
	165-295	-	-	-10.4	
	295-500	-	-	-2.9	
	500-700	-	-	-1.7	
	700-1100	-	720	-	

Table 6.1. Assigning events in the DTA/TGA curves to the samples studied.

From the comparison of the DTA/TGA curves obtained for all samples, it is observed that the sample P3 has in the temperature range 20-165 ºC the lowest loss of mass and the lowest endothermic event due to the elimination of the absorbed water, and the elimination of ethanol occurs at a higher temperature compared to the samples P0, P1 and P2. (Fig. 6.2.).

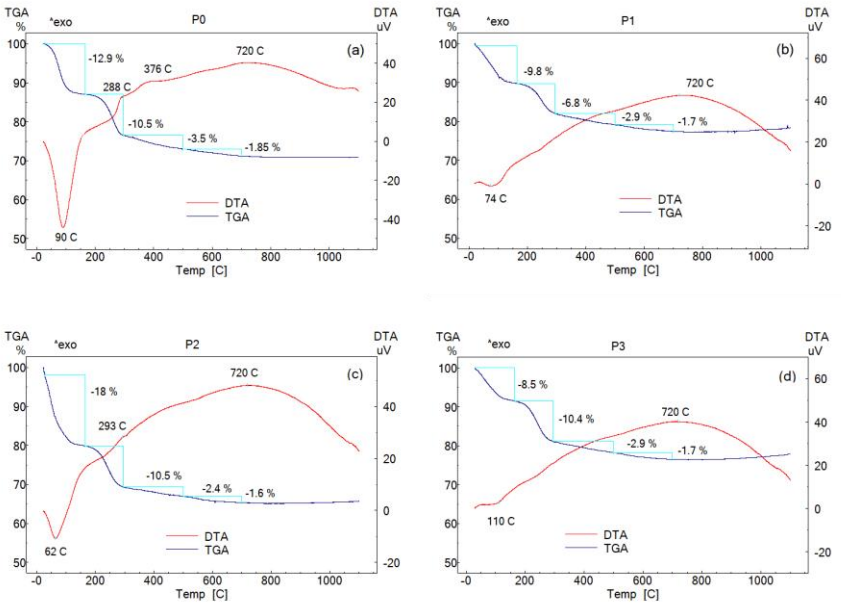

Figure 6.2. DTA/TGA curves of the samples studied.

Between 165 and 500 ºC, the DTA curve obtained for sample P0 (Fig. 6.2. P0.) contains two exothermic signals with the maximum at 288 and 376 ºC. These events and the corresponding mass loss ~ 14 % can be attributed to the decompositions [33] [34] and the burning reaction of the organic residues that remained after the synthesis process [35][36]. The small exothermic event with a maximum of 720 ºC, which occurs without a loss of mass, could be attributed to the dihydroxy and condensation of silanol from silica networks [33], [36]. This signal is also present in the DTA curves obtained for samples P1, P2 and P3. (Figure 6.2. P1, P2, P3) Additional heating up to 1100 ºC did not indicate the presence of the crystallization phenomenon in any of the samples investigated.

Based on the results of the thermal analysis, the samples were heat treated at 600 ºC for 1 hour to remove organic residues and achieve stability of the amorphous state of the samples.

X-ray diffraction

The X-ray diffractograms of the samples both after synthesis, but also after DTA and heat treatment indicate the amorphous nature of the biomaterial, both of the silica structure and of those doped with Dy and Gd, the amorphous property being confirmed by the wide peak at 23o characteristic of silica particles [37].

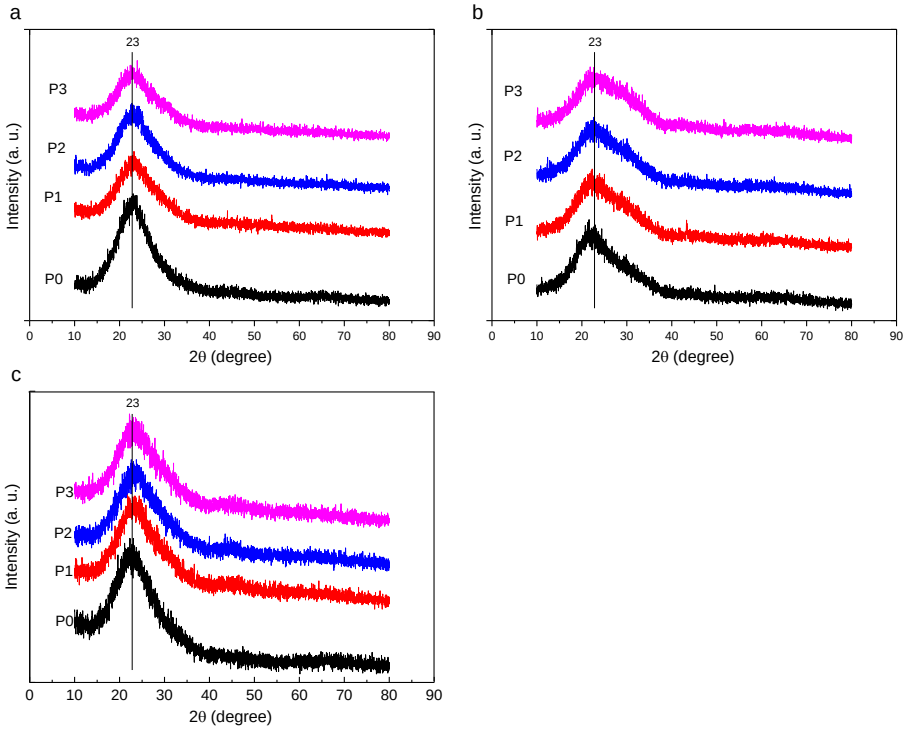

Figure 6.3. Diffractograms of the prepared samples: (a) as-prepared, (b) DTA/TGA (1100°C), (c) heat treatment from 600°C.

IR spectroscopy

The result of the FT-IR analyses obtained, in the range of 4000–400 cm-1, for samples before heat treatment is illustrated in Figure 6.4.a, and those after calcination are pre-formulated in Figure 6.4.b.

The major characteristics of the FT-IR spectra for all samples are the peaks at 1628, 1092, 974 and 459 cm-1 and are characteristic of the network vibration modes in a SiO2 matrix [38]. The bands

from d1224 and 1066 cm^{-1} are allocated to the asymmetrical stretching modes Si–O–Si [39]. The bands from 812 and 443 cm^{-1} are associated with the stretching/vibration and bending of the structure of the Si–O–Si network [40][41]. The results showed that the height of the peak corresponding to the Si-O-Si stretch vibration band (~1092 cm^{-1}) decreased in intensity in the case of samples doped with Gd and Dy.

In the case of FT-IR spectra corresponding to the samples prior to heat treatment, specific signals of the symmetrical stretching modes of the CH2 groups (2785 cm^{-1}) and those of simeric stretching present at infrared values of 2850 cm^{-1} are observed [42]. These specific characteristics of the spectra of non-heat-treated samples are no longer found in those after treatment, which supports the purity of the silica matrix in both the standard sample and those doped with paramagnetic ions.

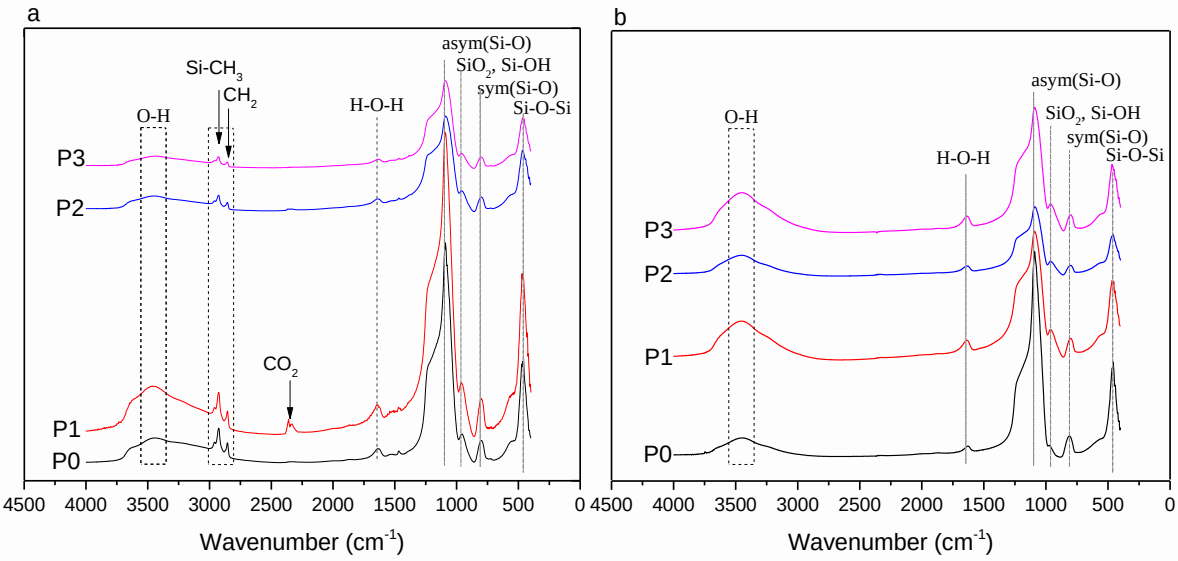

Figure 6.4 FT-IR spectra of samples (a) before heat treatment and (b) after heat treatment at 600 °C

Electronic paramagnetic resonance

The EPR spectra of the samples after preparation are illustrated in Figure 5 P1, P2,P3, and those after the heat treatment are represented in Figure 5 P1-TT, P2-TT, P3-TT.

The spectra of the sample doped with Dy3+ (Figure 5-P1 and P1-TT) do not show any indications of its EPR signal at room temperature, according to literature [38], [43] . The very

weak EPR signal present in the obtained spectrum can be attributed to possible impurities present in the precursors used in the sample synthesis.

The X-band EPR spectra obtained for samples containing only gadolinium (Figure 6.5 P2 and P2-TT) are characterised by four relatively low lines with effective g-values of 6; 4,8; 2.8 and 2 and can be attributed to Gd3+ ions in places with strong, intermediate and weak crystalline fields. The shape of the EPR spectrum of the Gd3+ ion (S = 7/2) exhibits a certain degree of complexity and has been called the "U" spectrum [44] [45] due to the "ubiquity" of this spectral form in various disordered materials [44] [45][46] [47]. The poorly resolved lines in geff ≈ 4.8 and 2.8 could be due to poor crystallization, while the dominant line in geff ≈ 2 appears from Gd3+ ions that mainly experience dipole interactions [48][49][50]. At the same time, this very wide line reflects the local disorder surrounding these paramagnetic ions., but most of them are strongly coupled forming clasters.

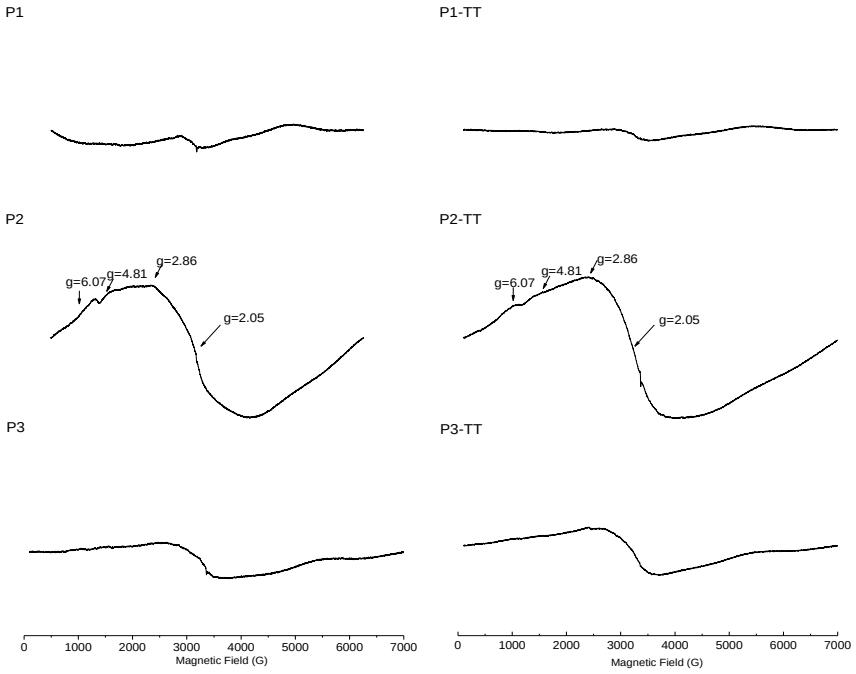

Figure 6.5. EPR spectra of the studied samples; a-c- non-heat-treated samples and d-f spectra of heat-treated samples

The EPR spectrum for the sample with Gd-Dy (Figure 6.5 P3 and P3-TT) shows the predominant characteristics of the paramagnetic ions Gd3+, located in positions strongly distorted by the presence of $Dy3^{+}$ ions.

Nuclear magnetic resonance

The ^{29}Si MAS-MRI spectra of the heat-treated samples can be decomposed into two signals at -100 and -110 ppm, which are assigned to si(Q_3) and Si(Q_4) units, and in the case of sample P2, si(Q_2)Si units [51][52) are also identified. The broad lines of resonance of the ^{29}Si MAS NMR spectra are determined by the amorphous character of the samples [53]. The influence of the composition on the local structure of the samples is evidenced by changes in the chemical displacement (ppm), in the width of the lines at half the maximum intensity of FWHM (ppm) and of the Qn fraction (%) resulting from the deconvolution of the spectra. The deconvolution of the experimental spectra were simulated by Gaussian functions in dmfit software [54] to obtain the distributions of the structural groups that derived from the area below each component, and the results of the separation of the vertices are shown in Table 5.2. According to the simulation results of the experimental spectra, the share of the Q4 and Q3 units in the P0 sample is approximately 50%, proportions that change significantly in the case of samples to which paramagnetic ions have been added (a peculiarity is present by the Si (Q_2) units. One possible explanation is that the surface of silica particles becomes more hydrophobic, the results being in line with the data from the literature [55].

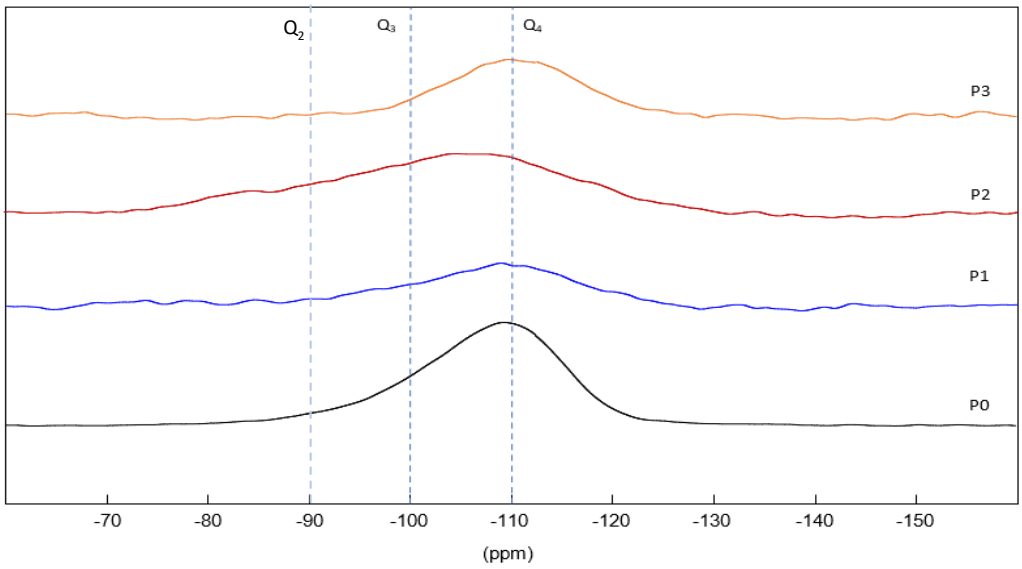

Figure 6.6 Spectra ^{29} Si MAS NMR

Sample	Q^n	δ (ppm)	FWHM (ppm)	Fq^n (%)
P0	Q^3	-104.1	15.3	51.2
	Q^4	-111.1	10.4	48.8
P1	Q^3	-99.9	18.44	30.3
	Q^4	-110.4	14.1	69.7
P2	Q^2	-93.1	16.2	26.2
	Q^3	-104.4	13.9	49.5
	Q^4	-112.5	11.3	24.3
P3	Q^3	-106.4	10.8	43.6
	Q^4	-112.9	10.9	56.4

Table 6.7 MRI parameters of simulated Qn lines from 29Si MAS MRI spectra of samples P0, P1, P2, P3.

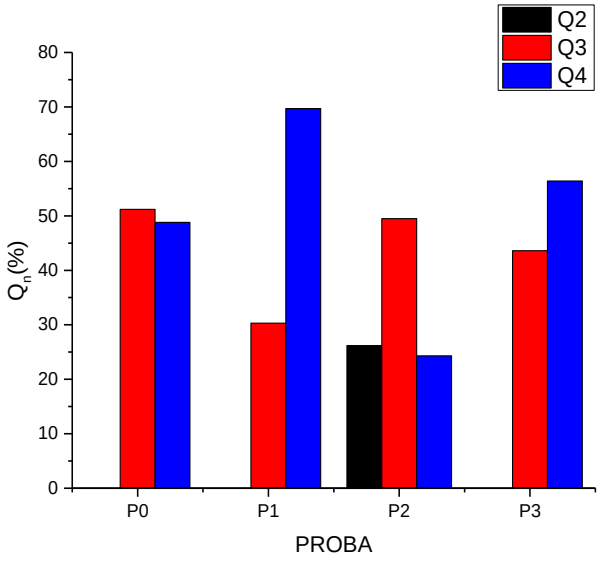

Fig.6.8. Dependence of the Qn fraction (%) of the samples P0,P1,P2,P3

Scanning electron microscopy

SEM analyses on heat-treated samples were divided into two stages, in the first stage the analyzes were made on the powdered samples, and in the second stage, the samples were immersed in water solution in containers of 0.5 mL, and then placed in the ultrasonic bath for 30 minutes. After this time interval, the solution was extracted by pipette one drop at a time and placed on the standard carbon support used in THE SEM analyses. Before being placed in the analysis chamber of the apparatus, the samples were dried at room temperature. The purpose of this second stage was to create a method of selection of silica microspheres in terms of size.

The images obtained in the first stage are shown in Figure 6.9. They show the high degree of agglomeration and the high variation in size of these silica spheroids doped with paramagnetic ions.

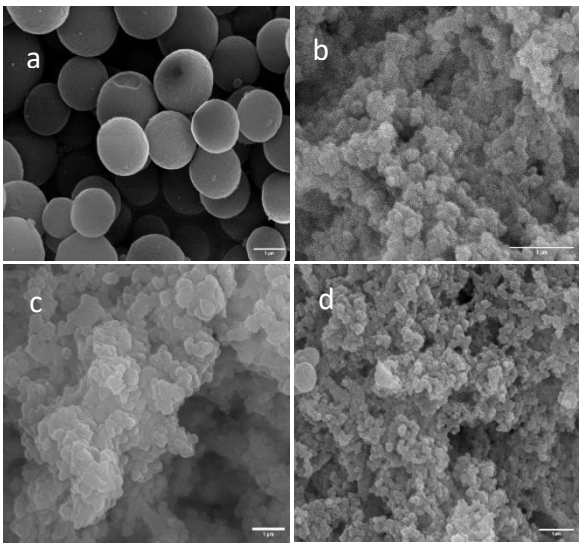

Figure 6.9. SEM images of powdered samples. (a- sample P0, b- sample P1, c-sample P2, d-sample P3

Figure 6.10 shows the images obtained by SEM in the case of samples synthesized by the modified Stober method, in the case of the sample P0 they are in spherical form and their size varies in the range from 1 μm to 2 μm. In the case of samples where paramagnetic ions (P1,P2,P3) have also been added, the unevenly distributed agglomerated spherical particles of a much smaller size compared to the P0 samples shall be identified.

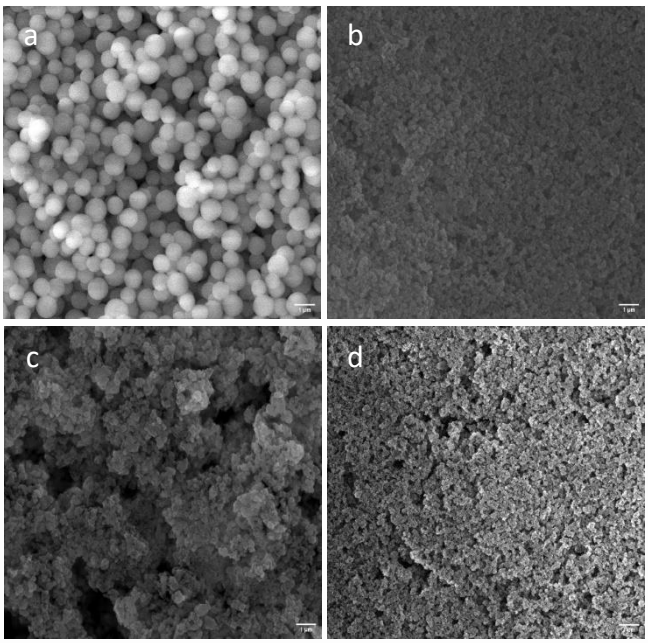

Figure 6.10. SEM images of samples extracted from the water solution after the ultrasound bath. (a- sample P0, b- sample P1, c-sample P2, d-sample P3

Transmission electron microscopy

TEM was performed on the P3 sample in powder form (SiO2 spheroids doped with Dy and Gd ions), both on the sample before heat treatment and after calcination.

The morphology of P3 spheroids before heat treatment is illustrated in Figure 6.11.a. Using the Selected Area Electron Diffraction (SAED) technique, it allowed the evaluation of the sample from the point of view of amorphous proprietary structures proven by the absence of light points and rings generated by electron diffraction, a phenomenon that would be created by the interaction of the beam with the atoms of the crystalline sample. This analysis is consistent with the results obtained by the DRX analyses.

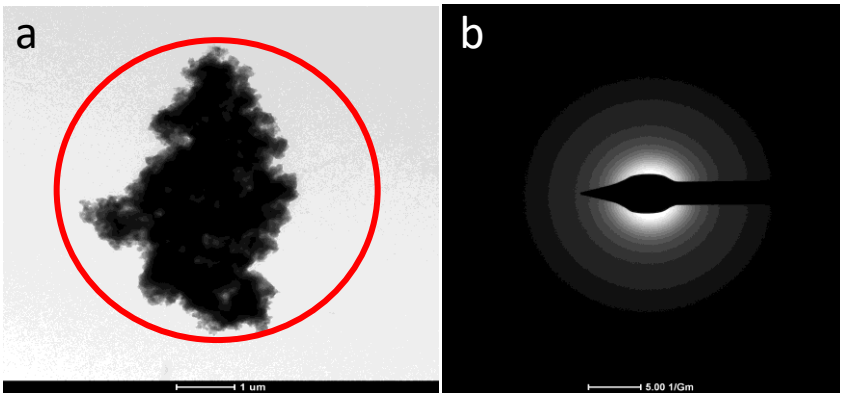

Figure 6.11.a. TEM images of the P3 sample before the thermal treatment.

b. SAED: diffraction of electrons in the selected area.

For the confirmation of the formation of silicate structure with Dy and Gd ions, EDX analysis was performed. During the measurement of EDX, different areas were focused (Figure 6.12 - sample P3 not heat treated). Figure 6.12 illustrates the EDX spectrum of sample P3, before calcination, from which the presence of both Dy and Gd atoms can be seen. Details of the EDX spectrum of the P3 sample measured in atomic and mass percentages can be found in Table 6.13.

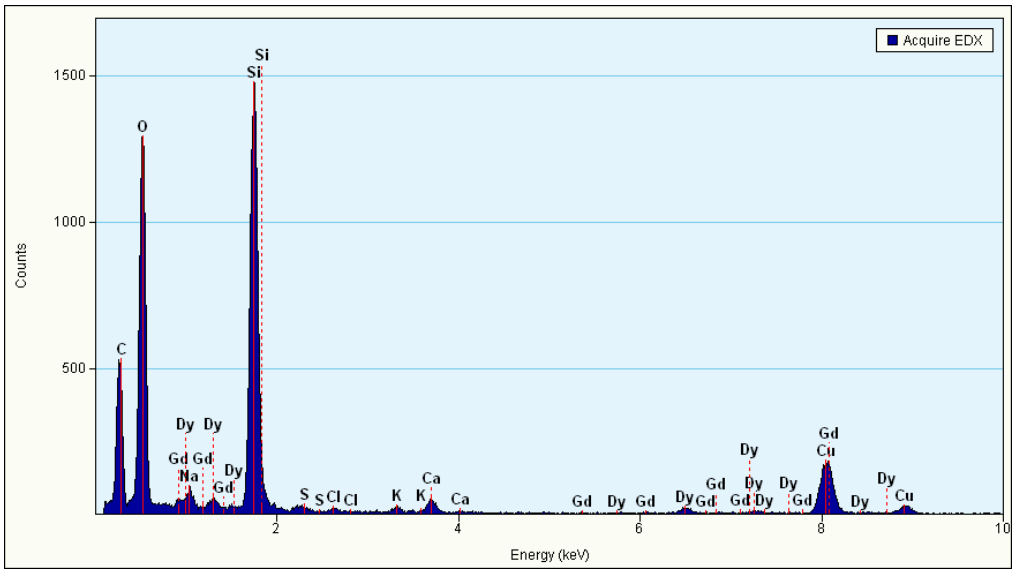

Figure 6.12. EDX spectrum of the P3 sample before heat treatment

EDX					
Element	Weight %	Atomic %	Uncert. %	Correction	k-Factor
O(K)	57.11	71.07	0.44	0.51	1.889
Si(K)	40.37	28.61	0.27	0.92	1
Gd(L)	0.09	0.002	0.04	0.99	3.483
Dy(L)	2.49	0.3	0.09	0.99	3.507

Table 6.13 Details of the EDX spectrum of the P3 sample before heat treatment

The TEM technique was also used for sample P3 (powder sample) after heat treatment was applied (Figure 6.14) and the EDX results from two different dust zones are given in Tables 6.15 and Table 6.16 respectively.

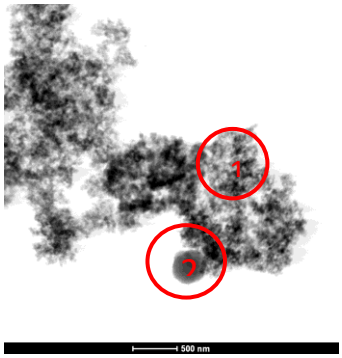

Figure 6.14. TEM images of the P3 sample after heat treatment

EDX1					
Element	Weight %	Atomic %	Uncert. %	Correction	k-Factor
O(K)	56.25	72.18	0.38	0.51	1.889
Si(K)	36.86	26.94	0.22	0.92	1
Gd(L)	0.97	0.12	0.04	0.99	3.483
Dy(L)	5.89	0.74	0.12	0.99	3.507

Table 6.15 Details of the EDX spectrum of the P3 sample after heat treatment

EDX2					
Element	Weight %	Atomic %	Uncert. %	Correction	k-Factor
O(K)	56.35	70.25	0.43	0.51	1.889
Si(K)	41.51	29.48	0.26	0.92	1
Gd(L)	0.69	0.08	0.04	0.99	3.483
Dy(L)	1.43	0.17	0.07	0.99	3.507

Table 6.16. Details of the EDX spectrum of the P3 sample after heat treatment

Elementary mapping using the HAADF-STEM-EDX technique revealed the distribution of Dy and Gd ions in the silica matrix. The corresponding picture of microscopy (HAADF-STEM) is shown in Figure 12(a). Haadf-STEM-EDX mapping analysis using the Si, Dy, and Gd energies shown in Fig. 7b–d describes the uniform elementary distribution of Dy and Gd in silica networks.

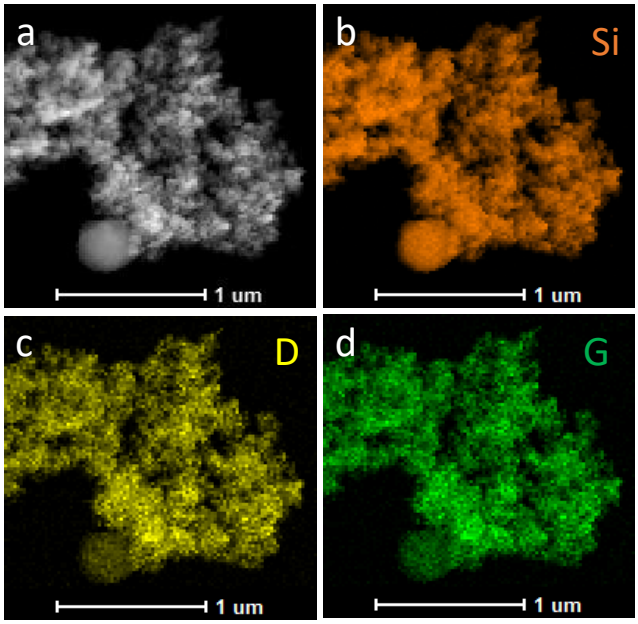

Figure 6.17. (a) HAADF-STEM-EDX map of a selected area of the image. (b) MAP HAADF-STEM-EDX Si. (c) Map HAADF-STEM-EDX Dy. (d) Map HAADF-STEM-EDX Gd

TEM results, both morphological and spectral images, and analyses of the elements showed the amorphous character of silica powder doped with Dy and Gd, but also the integration of these paramagnetic ions into the SiO2 network.

Determination of dimensional distribution and electrical potential

Particle size influences the properties of biomaterials that are in the form of particles and is a valuable indicator of their quality and performance in fulfilling their purpose as a contrast agent. The size and shape of the powders influences the flow and compaction properties. Larger, more spherical particles will usually flow more easily than smaller particles. Smaller particles dissolve faster and lead to higher suspension viscosities than larger particles. Smaller particle sizes and larger surface load (potential zeta) will usually improve suspension and emulsion stability [56].

The Zeta potential is a measure of the size of the electrostatic rejection or attraction of particles immersed in a liquid suspension. It is one of the fundamental parameters that are known to affect the stability of dispersion. The Zeta potential measurement provides a detailed insight into the causes of dispersion, aggregation or flocculation and can be applied to improve the formulation of dispersions, emulsions and suspensions [57].

Zeta's potential is one of the factors mediating interactions between particulate matter. Particles with a high Zeta potential (of positive or negative charge) repel each other (< 30 mV and >+30 mV are considered high Zeta potential values). For particles that are small enough and whose density is low enough to remain in suspension, a high Zeta potential provides stability, i.e. particulate matter resists aggregation [58].

In this experiment, the sample suspensions obtained by immersing them in water solution in the ultrasonic bath were used for 30 minutes.

In experiments to determine zeta potential, P0 and P3 samples were used. The results for both samples showed that the potential values are high (-39mV in the case of sample P0 and -33 mV in the case of sample P3), i.e. they form stable suspensions and the particles do not clutter under the conditions of the experiment, these results are illustrated in Figure 6.19 in which the three measurements can be identified at a time interval of 5 min for each sample.

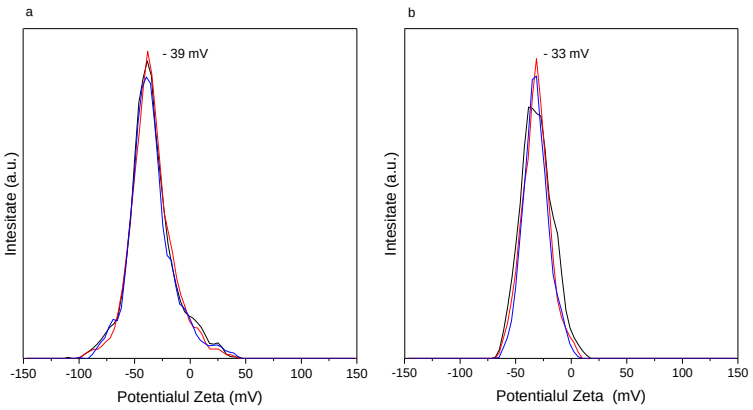

Figure 6.19. Zeta potential for samples P0 (a) and P3 (b)

The stability of silica microspheres is analyzed by measuring the dynamic light scattering (DLS). The colloidal stability of the mesoporous silica is discussed sporadically in the literature; in any case, the hydrodynamic diameter may affect the relaxationometry itself, the bonds of paramagnetic contrast agents and must be adequately and systematically reported [59].

The average hydrodynamic diameter is shown in Figure 6.20. The analyses performed on all samples, at intervals of 5 minutes, demonstrated greater stability in suspension of silica microspheres doped with paramagnetic ions.

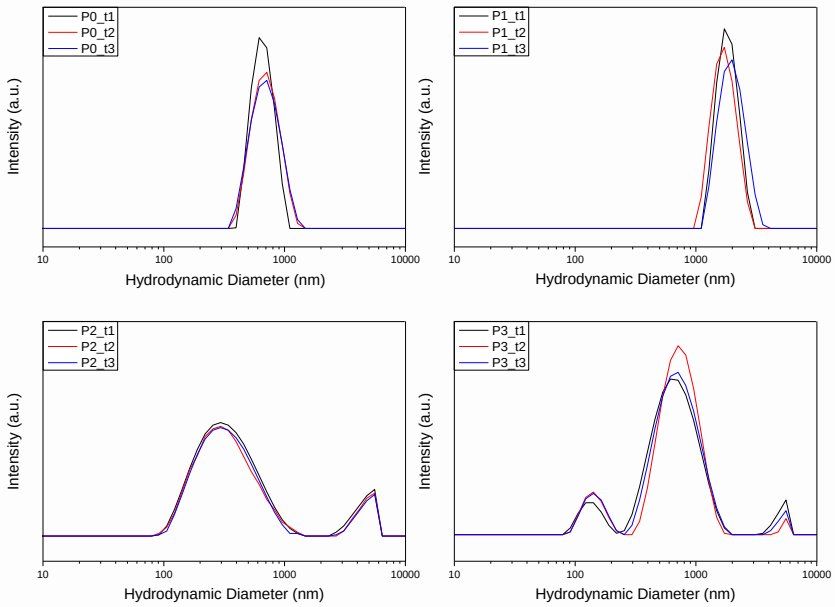

Figure 6.20. Hydrodynamic diameter of samples resulting from DLS measurements

Relaxometry by magnetic resonance imaging (R-MRI)

In the case of the MRI-relaxivity investigation, it was necessary to introduce a new sample ID to highlight the concentration of the solution (Table 2).

Figure 6.21 shows the T1- or T2-weighted MRI images, depending on the sample analysed. The negative contrast agent character of the P1 sample is supported by the T2-weighted image in which the decrease in the intensity of the MRI signal is observed by decreasing the transverse relaxation time, as well as the correlation between the "blackening" of the image and the concentration of the sample. The reverse effect (image illumination) is observed in the T1-weighted MRI images obtained on P2 samples. In the case of P3 samples, the effect of the contrast agent is much more visible in the case of T2-weighted images is due to the significantly higher concentration of Dy ions.

The relaxivity of r1 (longitudinal water proton relaxivity) and r2 (transverse water proton relaxivity) is defined as the slope of linear regression generated from the measured relaxation rate graph (1/Ti, where i=1, 2) relative to the AC concentration.[60].

Figure 6.22 shows the graphs of the inverse value of the easing times, depending on the concentration of the solutions in g/ml.

The values r1 and r2 for the samples analysed are found in Table 3. For the sample P1 it has a high value r2 which is due to the Dy ions that are paramagnetic so that the character of the negative contrast agent is highlighted [61]. Sample P2 has a high r1 value that supports its character as a positive contrast agent [62]. In the case of the sample P3, the high values r1 and r2 (Table 3) show clear improvements in concentration-dependent contrast showing the potential to act as a dual-mode MRI contrast agent for T1 and T2[19].

The general relaxivity ratio r2/r1 characterizes the contrast agent in such a way that a ratio with $r2/r1 < 10$ is a positive agent [63]. The contrast agent character is also supported by the values of this ratio (r2/r1) for both sample P1 and sample P2, and in the case of sample P3 it has an intermediate ratio r2/r1 and with high significant values of r1 and r2 which makes it suitable for dual contrast agent MRI, these results are consistent with previous results [19][61] [64][65][66].

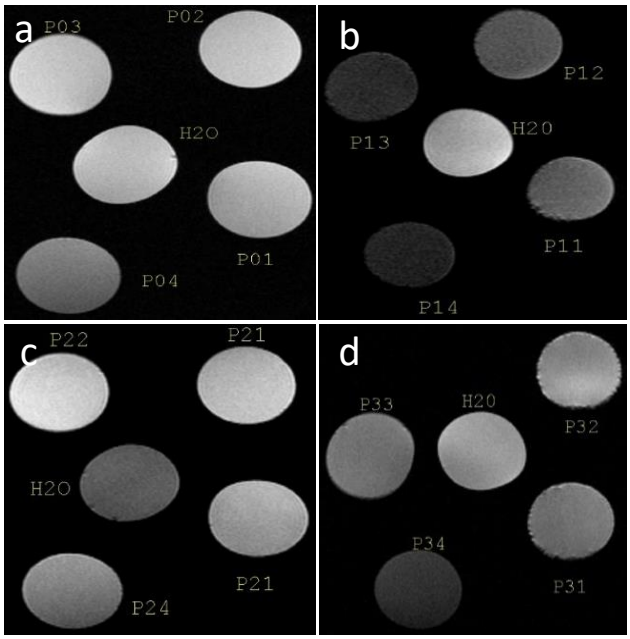

Figure 6.21. T1- and T2-weighted magnetic resonance images of the H2O reference solution and suspension sample P0,P1,P2,P3 with a concentration of 0,0015; 0,0035; 0,0055 0,0075 g/ml.

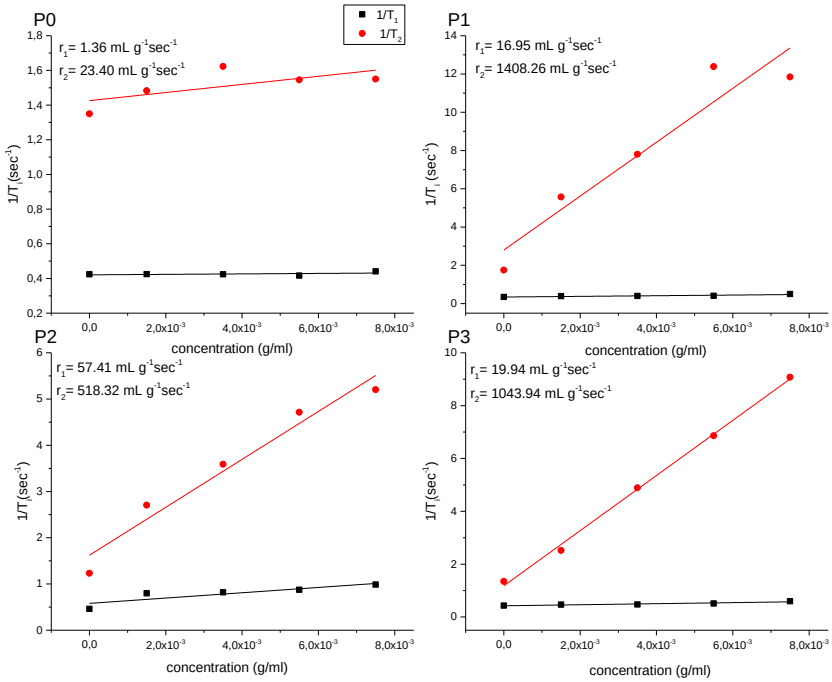

Figure 6.22. Graphs 1/T1 and 1/T2 of suspensions of aqueous samples according to concentrations of paramagnetic ions (g/ml). The slopes shown in each diagram correspond to the relaxations r1 and r2.

Sample	r1	r2	r2/r1
P0	1.36	23.4	*17.21*
P1	16.95	1408.26	*83.08*
P2	57.41	518.32	*9.03*
P3	19.94	1043.94	*52.35*

Table 3. r1 and r2 values of the samples and the ratio of the easing rate r2/r1

Chapter 6. Conclusions

Both in vivo and ex vivo preclinical studies have shown the versatility of RM imaging used in various research projects. The information obtained with the help of this non-invasive and non-destructive technique has added value to these the research. The information obtained through the use of this technique allowed for highlighting the different stages of development of the human nervous system, but also its use for the post-mortem diagnosis of embryonic congenital malformations being an alternative to classical autopsy. The observation of the intermediate effects after implantation proved to be very important, so it was decided to continue with them in the clinical field. Preclinical in vivo research has shown that the use of the MRI technique is necessary regardless of whether pathologies or the pharmacokinetics of some drugs are studied in the animal model.

SiO2-based biomaterials with the addition of paramagnetic ions (Dy, Gd, and Dy-Gd) were synthesized using the modified Stöber method to obtain materials with potential contrast agent in magnetic resonance imaging.

Structural characterization analyses have shown an amorphous structure through the results of XRD and STEM properties leading to probable high biocompatibility of the samples. Very good thermal stability is shown by DTA analyses, a physical property important for the final applicability of these samples. Their spheroid form was illustrated by SEM analyses, and the integration of paramagnetic ions into the silicate structure was demonstrated by 29Si MAS NMR,

EPR, FTIR spectroscopic, and TEM analyses that highlighted the relatively uniform distribution of paramagnetic ions in the silica matrix.

Their electrical potential demonstrated the ability of these samples not to agglomerate. Also, their stability in the suspension of micro-spheroids demonstrated their ability to remain in suspension, a property necessary for a contrast agent used in MR imaging.

The MR examinations of the samples showed a high rate of relaxivity for the P1 sample making it suitable as an MR T2 contrast agent. In the case of the P2 sample, it proved to be an effective contrast agent for T1, and in the case of P3 samples, the results showed that it is suitable for contrast in T1 and T2 weighted images, which demonstrates the character of a dual contrast agent. The relaxometry properties of these samples are also supported by the value of the ratio r2/r1 for all three samples, which qualifies them to be used as contrast agents. The results confirm the sustainability of applications as an MRI contrast agent in both T1 and T2-weighted imaging for all three synthesized systems.

All these results lead to new research perspectives on these samples, being necessary for biocompatibility analyses by immersion in SBF and analysis of the stability of paramagnetic ions in the silica matrix, and subsequently the realization of a protocol for preclinical in vivo investigations.

Bibliography

[1] X. Y. Zheng, J. Pellico, A. A. Khrapitchev, N. R. Sibson, and J. J. Davis, “Dy-DOTA integrated mesoporous silica nanoparticles as promising ultrahigh field magnetic resonance imaging contrast agents,” *Nanoscale*, vol. 10, no. 45, pp. 21041–21045, 2018, doi: 10.1039/c8nr07198e.

[2] Boitor-Borza, D; Crivii, Carmen; **Farcasanu, S**; Stamatian, F; "Morphology of the human brain in the embryonic period: anatomical study and assessment by 7T magnetic resonance imaging" *Obstetrica şi Ginecologia*,63,,47-52,2015,.

[3] D. Boitor-Borza, F. Turcu, **S. Farcasanu**, and C. Crivii, “Early development of human ganglionic eminences assessed in vitro by using 7.04 Tesla micro-MRI – a pilot study,” *Med. Pharm. Reports*, vol. 94, no. 1, pp. 35–42, 2021, doi: 10.15386/mpr-1715.

[4] D. Vulturar, **A. Farcaşanu**, F. Turcu, D. Boitor, and C. Crivii, “The volume of the cerebellum in the second semester of gestation,” *Clujul Med.*, vol. 91, no. 2, pp. 176–180,

2018, doi: 10.15386/cjmed-922.

[5] A. Staicu, **A. S. Farcasanu**, G. Caracostea, R. V. F. Turcu, S. Simon, and F. Stamatian, "Contribution of post-mortem MRI to the evaluation of subtle renal anomalies in a first trimester foetus with Down syndrome," *J. Obstet. Gynaecol. (Lahore).*, vol. 36, no. 3, pp. 359–360, 2016, doi: 10.3109/01443615.2015.1065232.

[6] Popescu, Radu A; Tăbăran, Flaviu A; Bogdan, Sidonia**; Fărcășanu, Alexandru**; Purdoiu, Robert; Magyari, Klara; Vulpoi, Adriana; Dreancă, Alexandra; Sevastre, Bogdan; Simon, Simion;, "Bone regeneration response in an experimental long bone defect orthotopically implanted with alginate-pullulan-glass-ceramic composite scaffolds," *J. Biomed. Mater. Res. - Part B Appl. Biomater.*, vol. 108, no. 3, pp. 1129–1140, 2020, doi: 10.1002/jbm.b.34464..

[7] Cocan, Daniel; Mireşan, Vioara; Popescu, Florentina; Constantinescu, Radu; Coroian, Aurelia; Laţiu, Călin; Flaviu Turcu, Romulus Valeriu; **Fărcăşanu, Alexandru Ştefan**; Martonos, Cristian, "MRI investigations on venomous glands of brown bullhead, ameiurus nebulosus (Lesueur, 1819) (Actinopterygii: Ictaluridae)," *Pak. J. Zool.*, vol. 52, no. 4, pp. 1347–1354, 2020, doi: 10.17582/journal.pjz/20180717090711

[8] Antonela M. Berar, Dan Preda, Simona Iacob, Corina V. Moraru, **Alexandru Farcasanu**, Flaviu R. V. Turcu, Simion Simon, Smaranda Buduru " Assessment of periapical lesions by 7T magnetic resonance imaging and micro-CT - experimental study" *Human and Veterinary Medicine*; Cluj-Napoca Vol. 14, Iss. 1, (Mar 2022): 10-15

[9] **Alexandru Ștefan Fărcășanu**, Lăcrămioara Samoilă, Ovidiu Samoilă, Oliviu Voștinaru, Elena Dinte, Simion Simon, Ede Bodoki, "Assessment of the ocular biodistribution profile of topically administered lutein by magnetic resonance spectroscopy," , Comunicare orală la 12th International Symposium of Drug Analysis 32nd International Symposium on Pharmaceutical and Biomedical Analysis, Belgia ,vol. 46, no. 9, p. 2021, 2022.

[10] T. H. Shin *et al.*, "T 1 and T 2 dual-mode MRI contrast agent for enhancing accuracy by engineered nanomaterials," *ACS Nano*, vol. 8, no. 4, pp. 3393–3401, 2014, doi: 10.1021/nn405977t.

[11] S. Marasini *et al.*, "A Novel Paramagnetic Nanoparticle T2 Magnetic Resonance Imaging Contrast Agent With High Colloidal Stability: Polyacrylic Acid-Coated Ultrafine Dysprosium Oxide Nanoparticles," *Bull. Korean Chem. Soc.*, vol. 41, no. 8, pp. 829–836, 2020, doi: 10.1002/bkcs.12074.

[12] F. Wang, E. Peng, B. Zheng, S. F. Y. Li, and J. M. Xue, "Synthesis of Water-Dispersible Gd2O3/GO Nanocomposites with Enhanced MRI T1 Relaxivity," *J. Phys. Chem. C*, vol. 119, no. 41, pp. 23735–23742, 2015, doi: 10.1021/acs.jpcc.5b06037.

[13] G. Liu, N. M. K. Tse, M. R. Hill, D. F. Kennedy, and C. J. Drummond, "Disordered mesoporous gadolinosilicate nanoparticles prepared using gadolinium based ionic liquid emulsions: Potential as magnetic resonance imaging contrast agents," *Aust. J. Chem.*, vol. 64, no. 5, pp. 617–624, 2011, doi: 10.1071/CH11064.

[14] F. X. Wan, T. K. Zhang, Y. Li, C. C. Li, and L. Jiang, "Synthesis and study on magnetic

resonance imaging performance of Gd(III)-DTPA-bisbenzothiazol hydrazide," *J. Chil. Chem. Soc.*, vol. 61, no. 2, pp. 2861–2863, 2016, doi: 10.4067/S0717-97072016000200003.

[15] I. Bertini, C. Luchinat, G. Parigi, and E. Ravera, *Relaxometry and contrast agents for MRI*. 2017.

[16] J. S. Choi, J. H. Lee, T. H. Shin, H. T. Song, E. Y. Kim, and J. Cheon, "Self-confirming 'aND' logic nanoparticles for fault-free MRI," *J. Am. Chem. Soc.*, vol. 132, no. 32, pp. 11015–11017, 2010, doi: 10.1021/ja104503g.

[17] J. Fang *et al.*, "Manipulating the surface coating of ultra-small Gd2O3 nanoparticles for improved T1-weighted MR imaging," *Biomaterials*, vol. 35, no. 5, pp. 1636–1642, 2014, doi: 10.1016/j.biomaterials.2013.11.032.

[18] S. Wan *et al.*, "Dysprosium-Modified Gold Nanoparticles as T2exContrast Agents for Magnetic Resonance Imaging," *ACS Appl. Nano Mater.*, vol. 3, no. 9, pp. 9433–9439, 2020, doi: 10.1021/acsanm.0c02044.

[19] T. Tegafaw *et al.*, "Dual-mode T1 and T2 magnetic resonance imaging contrast agent based on ultrasmall mixed gadolinium-dysprosium oxide nanoparticles: Synthesis, characterization, and in vivo application," *Nanotechnology*, vol. 26, no. 36, 2015, doi: 10.1088/0957-4484/26/36/365102.

[20] M. Borges *et al.*, "Dual T1/T2 MRI contrast agent based on hybrid SPION@coordination polymer nanoparticles," *RSC Adv.*, vol. 5, no. 105, pp. 86779–86783, 2015, doi: 10.1039/c5ra17661a.

[21] J. Wang *et al.*, "An Ultrahigh-Field-Tailored T1–T2 Dual-Mode MRI Contrast Agent for High-Performance Vascular Imaging," *Adv. Mater.*, vol. 33, no. 2, pp. 1–8, 2021, doi: 10.1002/adma.202004917.

[22] Y. Mehmood *et al.*, "Facile synthesis of mesoporous silica nanoparticles using modified sol-gel method: Optimization and in vitro cytotoxicity studies," *Pak. J. Pharm. Sci.*, vol. 32, no. 4, pp. 1805–1812, 2019.

[23] M. Vallet-Regi, A. Rámila, R. P. Del Real, and J. Pérez-Pariente, "A new property of MCM-41: Drug delivery system," *Chem. Mater.*, vol. 13, no. 2, pp. 308–311, 2001, doi: 10.1021/cm0011559.

[24] P. P. Ghimire and M. Jaroniec, "Renaissance of Stöber method for synthesis of colloidal particles: New developments and opportunities," *J. Colloid Interface Sci.*, vol. 584, no. xxxx, pp. 838–865, 2021, doi: 10.1016/j.jcis.2020.10.014.

[25] W. Stober, A. Fink, and A. E. Bohn, "Controlled Growth of Monodisperse Silica Spheres in the Micron Size Range 1," *J. Colloid Interface Sci.*, vol. 26, pp. 62–69, 1968.

[26] O. C. Drăgan, A. Ş. Fărcăşanu, R. S. Câmpian, and R. V. F. Turcu, "Human tooth and root canal morphology reconstruction using magnetic resonance imaging," *Clujul Med.*, vol. 89, no. 1, pp. 137–142, 2016, doi: 10.15386/cjmed-555.

[27] M. Todea, M. Muresan-Pop, V. Simon, A. Vulpoi, and S. Simon, "Synthesis and

characterization of composite SiO2–Al2O3–Fe2O3 core–shell microspheres," *J. Sol-Gel Sci. Technol.*, vol. 96, no. 2, pp. 395–404, 2020, doi: 10.1007/s10971-020-05346-4.

[28] S. Ebnesajjad, *Surface and material characterization techniques*. Elsevier Inc., 2011.

[29] "Simultaneous Thermogravimetry/ Differential Thermal Analyzer." https://www.ssi.shimadzu.com/products/thermal-analysis/simultaneous-thermal-analysis/dtg-60-series/index.html (accessed Jun. 22, 2022).

[30] "MRI.jpg (2000×1125)." http://phys.ubbcluj.ro/laboratoare/cnrm/imagini/MRI.jpg (accessed Jun. 22, 2022).

[31] "pMRI - Parametric MRI | Medical Imaging Software | Philadelphia." https://www.parametricmri.com/ (accessed Mar. 16, 2022).

[32] "OriginLab - Origin and OriginPro - Data Analysis and Graphing Software." https://www.originlab.com/ (accessed Mar. 16, 2022).

[33] S. Yousatit, T. Jittapasata, N. Leelaphattharaphan, S. Nuntang, and C. Ngamcharussrivichai, "One-pot synthesis of wormhole-like mesostructured silica with a high amine loading for enhanced adsorption of clofibric acid," *J. Porous Mater.*, vol. 25, no. 6, pp. 1611–1623, 2018, doi: 10.1007/s10934-018-0575-6.

[34] M. Todea a , V. Simon , M. Muresan-Pop , A. Vulpoi , M.M. Rusu , A. Simion d , M. Vasilescu, G. Damian c , D.M. Petrisor , S. Simon "Silica-based microspheres with aluminum-iron oxide shell for diagnosis and cancer treatment," *J. Mol. Struct.*, vol. 1246, p. 131149, 2021, doi: 10.1016/j.molstruc.2021.131149.

[35] J. Yu, L. Zhao, and B. Cheng, "Preparation of monodispersed microporous SiO2 microspheres with high specific surface area using dodecylamine as a hydrolysis catalyst," *J. Solid State Chem.*, vol. 179, no. 1, pp. 226–232, 2006, doi: 10.1016/j.jssc.2005.10.036.

[36] H. Zhao, Y. Xin, H. Wang, Z. Zhang, and S. Liu, "A Comparison of the Formation of SiO 2 Particles Under the Catalysis of Dodecylamine and Ammonia Solutions," *J. Inorg. Organomet. Polym. Mater.*, vol. 21, no. 4, pp. 925–928, 2011, doi: 10.1007/s10904-011-9541-3.

[37] R. S. Dubey, Y. B. R. D. Rajesh, and M. A. More, "Synthesis and Characterization of SiO2 Nanoparticles via Sol-gel Method for Industrial Applications," *Mater. Today Proc.*, vol. 2, no. 4–5, pp. 3575–3579, 2015, doi: 10.1016/j.matpr.2015.07.098.

[38] E. Moncada, R. Quijada, J. Retuert, E. Moncada, R. Quijada, and J. Retuert, "Nanoparticles prepared by the sol gel method and their use in the formation of nanocomposites with polypropylene," *Nanot*, vol. 18, no. 33, p. 335606, Aug. 2007, doi: 10.1088/0957-4484/18/33/335606.

[39] C. J. Brinker and G. W. Scherer, *Sol-gel science : the physics and chemistry of sol-gel processing*. Academic Press, 1990.

[40] N. D. Singho and M. R. Johan, "Complex impedance spectroscopy study of silica nanoparticles via sol-gel method," *Int. J. Electrochem. Sci.*, vol. 7, no. 6, pp. 5604–5615, 2012.

[41] D. Eniu, C. Gruian, E. Vanea, L. Patcas, and V. Simon, “FTIR and EPR spectroscopic investigation of calcium-silicate glasses with iron and dysprosium,” *J. Mol. Struct.*, vol. 1084, pp. 23–27, 2015, doi: 10.1016/j.molstruc.2014.12.020.

[42] “Infrared Spectroscopy.” https://www2.chemistry.msu.edu/faculty/reusch/virttxtjml/spectrpy/infrared/infrared.htm (accessed Jun. 28, 2022).

[43] B. P. Kore *et al.*, “Thermoluminescence and EPR study of K2CaMg(SO4)3:Dy phosphor: The dosimetric application point of view,” *J. Phys. D. Appl. Phys.*, vol. 49, no. 9, 2016, doi: 10.1088/0022-3727/49/9/095102.

[44] T. Mashiko *et al.*, “EPR of Gd3+ with g≈6.0 in glasses: a reinterpretation,” *J. Phys. C Solid State Phys.*, vol. 15, no. 26, p. L933, Sep. 1982, doi: 10.1088/0022-3719/15/26/010.

[45] C. M. Brodbeck and L. E. Iton, “The EPR spectra of Gd3+ and Eu2+ in glassy systems,” *J. Chem. Phys.*, vol. 83, no. 9, p. 4285, Aug. 1998, doi: 10.1063/1.449041.

[46] S. Simon and A. D. Udvar, “Effect of gadolinium on the structure and magnetic properties of glass and glass-ceramic sillenites,” *J. Am. Ceram. Soc.*, vol. 93, no. 9, pp. 2760–2763, 2010, doi: 10.1111/j.1551-2916.2010.03783.x.

[47] S. Simon, R. Pop, V. Simon, and M. Coldea, “Structural and magnetic properties of lead-bismuthate oxide glasses containing S-state paramagnetic ions,” *J. Non. Cryst. Solids*, vol. 331, no. 1–3, pp. 1–10, Dec. 2003, doi: 10.1016/J.JNONCRYSOL.2003.08.079.

[48] S. Arora, V. Kundu, D. R. Goyal, and A. S. Maan, “Structure and magnetic properties of Bi2O3–GeO2–Gd2O3 glasses,” *ISRN Ceram.*, vol. 2013, pp. 1–5, 2013, doi: 10.1155/2013/914324.

[49] E. Culea, L. Pop, and S. Simon, “Spectroscopic and magnetic behaviour of xGd2O3 (1 - x)(Bi2O3·PbO) glasses,” *Mater. Sci. Eng. B Solid-State Mater. Adv. Technol.*, vol. 112, no. 1, pp. 59–63, 2004, doi: 10.1016/j.mseb.2004.06.001.

[50] M. Zagrai *et al.*, “Lead metallic-lead dioxide glasses as alternative of immobilization of the radioactive wastes,” *JNCS*, vol. 405, pp. 129–134, Dec. 2014, doi: 10.1016/J.JNONCRYSOL.2014.09.006.

[51] S. E. Ashbrook and D. M. Dawson, “NMR spectroscopy of minerals and allied materials,” *Nucl. Magn. Reson.*, vol. 45, pp. 1–52, 2016, doi: 10.1039/9781782624103-00001.

[52] H. Maekawa, T. Maekawa, K. Kawamura, and T. Yokokawa, “The structural groups of alkali silicate glasses determined from 29Si MAS-NMR,” *J. Non. Cryst. Solids*, vol. 127, no. 1, pp. 53–64, 1991, doi: 10.1016/0022-3093(91)90400-Z.

[53] A. Simion, M. Vasilescu, C. Filip, M. Todea, M. Mureșan-Pop, and S. Simon, “Structural characterization of interfaces in silica core-alumina shell microspheres by solid-state NMR spectroscopy,” *Solid State Nucl. Magn. Reson.*, vol. 117, no. October 2021, 2022, doi: 10.1016/j.ssnmr.2022.101773.

[54] “Home | dmfit - D.Massiot - NMR@CEMHTI CNRS UPR3079 Orléans France.” .

[55] Y. Cabrera, A. Cabrera, F. H. Larsen, and C. Felby, "Solid-state 29Si NMR and FTIR analyses of lignin-silica coprecipitates," *Holzforschung*, vol. 70, no. 8, pp. 709–718, 2016, doi: 10.1515/hf-2015-0165.

[56] C. Irvine, "a Guidebook To Particle Size Analysis," *Horiba*, pp. 1–17, 2019.

[57] Malvern, "A basic guide to particle characterization," *Malvern whitepaper*, pp. 1–24, 2015, [Online]. Available: https://www.cif.iastate.edu/sites/default/files/uploads/Other_Inst/Particle Size/Particle Characterization Guide.pdf.

[58] V. Feldmann, J. Engelmann, S. Gottschalk, and H. A. Mayer, "Synthesis, characterization and examination of Gd[DO3A-hexylamine]-functionalized silica nanoparticles as contrast agent for MRI-applications," *J. Colloid Interface Sci.*, vol. 366, no. 1, pp. 70–79, 2012, doi: 10.1016/j.jcis.2011.09.053.

[59] R. Guillet-Nicolas, J. L. Bridot, Y. Seo, M. A. Fortin, and F. Kleitz, "Enhanced relaxometric properties of MRI 'positive' contrast agents confined in three-dimensional cubic mesoporous silica nanoparticles," *Adv. Funct. Mater.*, vol. 21, no. 24, pp. 4653–4662, 2011, doi: 10.1002/adfm.201101766.

[60] M. Rohrer, H. Bauer, J. Mintorovitch, M. Requardt, and H. J. Weinmann, "Comparison of magnetic properties of MRI contrast media solutions at different magnetic field strengths," *Invest. Radiol.*, vol. 40, no. 11, pp. 715–724, 2005, doi: 10.1097/01.rli.0000184756.66360.d3.

[61] K. Kattel *et al.*, "Paramagnetic dysprosium oxide nanoparticles and dysprosium hydroxide nanorods as T 2 MRI contrast agents," *Biomaterials*, vol. 33, no. 11, pp. 3254–3261, 2012, doi: 10.1016/j.biomaterials.2012.01.008.

[62] L. Relaxivity *et al.*, "Paramagnetic Ultrasmall Gadolinium Oxide Nanoparticles as Advanced T1 MRI Contrast Agent: Account for Large Diameter, and In Vivo T1 MR Images," *ACS Nano*, vol. 3, no. 11, pp. 3663–3669, 2009.

[63] F. H. Wang, K. Bae, Z. W. Huang, and J. M. Xue, "Two-photon graphene quantum dot modified Gd2O3 nanocomposites as a dual-mode MRI contrast agent and cell labelling agent," *Nanoscale*, vol. 10, no. 12, pp. 5642–5649, 2018, doi: 10.1039/c7nr08068a.

[64] Q. L. Vuong *et al.*, "Paramagnetic nanoparticles as potential MRI contrast agents: Characterization, NMR relaxation, simulations and theory," *Magn. Reson. Mater. Physics, Biol. Med.*, vol. 25, no. 6, pp. 467–478, 2012, doi: 10.1007/s10334-012-0326-7.

[65] E. Gómez-Gónzalez *et al.*, "Dysprosium and Holmium Vanadate Nanoprobes as High-Performance Contrast Agents for High-Field Magnetic Resonance and Computed Tomography Imaging," *Inorg. Chem.*, vol. 60, no. 1, pp. 152–160, 2021, doi: 10.1021/acs.inorgchem.0c02601.

[66] R. Antwi-Baah, Y. Wang, X. Chen, and K. Yu, "Metal-Based Nanoparticle Magnetic Resonance Imaging Contrast Agents: Classifications, Issues, and Countermeasures toward their Clinical Translation," *Adv. Mater. Interfaces*, vol. 2101710, pp. 1–31, 2022, doi: 10.1002/admi.202101710.

Dissemination of the results

Papers ISI on thesis' subject:

1. Cocan, Daniel; Mireşan, Vioara; Popescu, Florentina; Constantinescu, Radu; Coroian, Aurelia; Laţiu, Călin; Flaviu Turcu, Romulus Valeriu; **Fărcăşanu, Alexandru Ştefan**; Martonos, Cristian; ,"*MRI Investigations on Venomous Glands of Brown Bullhead, Ameiurus nebulosus (Lesueur, 1819)(Actinopterygii: Ictaluridae).",*Pakistan Journal of Zoology,52,4,,2020, IF: 0.831 , AIS: 0.113
2. Popescu, Radu A; Tăbăran, Flaviu A; Bogdan, Sidonia**; Fărcășanu, Alexandru**; Purdoiu, Robert; Magyari, Klara; Vulpoi, Adriana; Dreancă, Alexandra; Sevastre, Bogdan; Simon, Simion; ,*Bone regeneration response in an experimental long bone defect orthotopically implanted with alginate-pullulan-glass-ceramic composite scaffolds*, Journal of Biomedical Materials Research Part B: Applied Biomaterials,108,3,1129-1140,2020,"John Wiley & Sons, Inc. Hoboken, USA", IF: 3.68 , AIS: 0.539
3. Staicu, **A; Farcasanu**, AS; Caracostea, G; Turcu, RV; Simon, S; Stamatian, F; ,*Contribution of post-mortem MRI to the evaluation of subtle renal anomalies in a first trimester foetus with Down syndrome*,J Obstet Gynaecol,36,3,359-60,2016, IF: 3.368 , AIS: 0.539

Papers ISI on thesis' subject:

1. **A.S. Farcasanu**, M. Todea, M. Muresan-Pop, D.M. Petrisor, A. Simion, A. Vulpoi, S. Simon; *Synthesis and structural characterization of silica particles doped with Dy and Gd paramagnetic ions for as MRI contrast agents*, Results in Chemistry (RECHEM-D-22-00527)
2. Boitor-Borza, Dan; Turcu, Flavius; **Farcasanu, Stefan**; Crivii, Carmen; ,*Early development of human ganglionic eminences assessed in vitro by using 7.04 Tesla micro-MRI–a pilot study*, Medicine and pharmacy reports,94,1,35,2021,"Universty of Medicine and Pharmacy of Cluj-Napoca, Romania"

3. Berar, Antonela M; Preda, Dan; Iacob, Simona; Moraru, Corina V; **Farcasanu, Alexandru**; Turcu, Flaviu RV; Simon, Simion; Buduru, Smaranda; ,*Assessment of*

periapical lesions by 7T magnetic resonance imaging and micro-CT-experimental study, Human and Veterinary Medicine,14,1,10-15,2022,Bioflux SRL

4. Vulturar, Damiana; **Fărcăşanu, Alexandru**; Turcu, Flaviu; Boitor, Dan; Crivii, Carmen; *The volume of the cerebellum in the second semester of gestation*, Clujul Medical,91,2,176,2018,"Universty of Medicine and Pharmacy of Cluj-Napoca, Romania"
5. Drăgan, Oana Carmen; **Fărcăşanu, Alexandru Ştefan**; Câmpian, Radu Septimiu; Turcu, Romulus Valeriu Flaviu; ,*Human tooth and root canal morphology reconstruction using magnetic resonance imaging,* Clujul Medical,89,1,137,2016,"Universty of Medicine and Pharmacy of Cluj-Napoca, Romania"
6. Boitor-Borza, D; Crivii, Carmen; **Farcasanu, S**; Stamatian, F; ,*Morphology of the human brain in the embryonic period: anatomical study and assessment by 7T magnetic resonance imaging*, Obstetrica şi Ginecologia,63,,47-52,2015.

Other articles published in ISI journals:

1. Aurel Jurjiu, Mircea Galiceanu**, Alexandru Farcasanu,** Liviu Chiriac, Flaviu Turcu; "*Relaxation dynamics of Sierpinski hexagon fractal polymer: Exact analytical results in the Rouse-type approachand numerical results in the Zimm-type approach*" The Journal of Chemical Physics 145, 214901 (2016); https://doi.org/10.1063/1.4968209, IF: 3.488 , AIS: 1.103
2. Morosanu, Cezar Octavian; Nicolae, Liviu; Moldovan, Remus; **Farcasanu, Alexandru** Stefan; Filip, Gabriela Adriana; Florian, Ioan Stefan; ,*Neurosurgical cadaveric and in vivo large animal training models for cranial and spinal approaches and techniques—a Ssystematic review of the current literature*, Neurologia i neurochirurgia polska,53,1,8-17,2019, IF: 2.223, AIS: 0.378

Conference participations on thesis' subject:

1. **Alexandru Ștefan Fărcășanu**, Lăcrămioara Samoilă, Ovidiu Samoilă, Oliviu Voștinaru, Elena Dinte, Simion Simon, Ede Bodoki *"Assessment of the ocular biodistribution profile of topically administered lutein by magnetic resonance spectroscopy" [DA-PBA 2022]:* Comunicare orală la 12th International Symposium of Drug Analysis 32nd International Symposium on Pharmaceutical and Biomedical Analysis, 2022 Belgia.

2. *Dan Boitor-Borza, C. Crivii, F. Turcu,* **A. Farcasanu,** S. Simon, F. Stamatian „*Morphogenesis of the human brain assessed by in vitro morcro-MRI „next generation"embryology*" XIII World Congress of Perinatal Medicine Belgrade – October 26-29, 2017.